One-pot synthesis of carboxymethyl-dextran coated iron oxide nanoparticles (CION) for preclinical fMRI and MRA applications

Manasmita Das[a,b,c,1,*], **Esteban A. Oyarzabal**[a,b,c,d,1], **Lars Chen**[a,b,c], **Sung-Ho Lee**[a,b,c], **Neal Shah**[a,b,c], **Gabby Gerlach**[a,b,c], **Weiting Zhang**[a,b,c], **Tzu-Hao Harry Chao**[a,b,c], **Nathalie Van Den Berge**[a,b,c,g], **Carolyn Liu**[a,b,c], **Carrie Donley**[e], **Stephanie A. Montgomery**[f], **Yen-Yu Ian Shih**[a,b,c,*]

[a]Center for Animal MRI, University of North Carolina, Center for Animal MRI, 125 Mason Farm Road, CB# 7513, Chapel Hill, NC 27599, USA

[b]Biomedical Research Imaging Center, University of North Carolina, Chapel Hill, NC, USA

[c]Department of Neurology, University of North Carolina, Chapel Hill, NC, USA

[d]Curriculum in Neurobiology, University of North Carolina, Chapel Hill, NC, USA

[e]Center for Nanotechnology in Drug Delivery, University of North Carolina, Chapel Hill, NC, USA

[f]Department of Pathology and Laboratory Medicine, University of North Carolina, Chapel Hill, NC, USA

[g]Medical Image and Signal Processing Group, Ghent University, Ghent, Belgium

Abstract

Superparamagnetic iron-oxide nanoparticles are robust contrast agents for magnetic resonance imaging (MRI) used for sensitive structural and functional mapping of the cerebral blood volume (CBV) when administered intravenously. To date, many CBV-MRI studies are conducted with Feraheme, manufactured for the clinical treatment of iron-deficiency. Unfortunately, Feraheme is currently not available outside the United States due to commercial and regulatory constraints, making CBV-MRI methods either inaccessible or very costly to achieve. To address this

*Corresponding authors at: Center for Animal MRI, 125 Mason Farm Road, CB# 7513, University of North Carolina, Chapel Hill, NC 27599, USA, dmanasmi@email.unc.edu (M. Das), shihy@unc.edu (Y.-Y.I. Shih).
[1]These authors contributed equally to this work.

Credit author statement

Manasmita Das: Conceptualization, Data curation, Formal analysis, Funding acquisition, Investigation, Methodology, Supervision, Validation, Visualization, Writing - original draft. **Esteban A. Oyarzabal:** Conceptualization, Data curation, Formal analysis, Investigation, Validation, Visualization, Writing - original draft. **Lars Chen:** Investigation, Methodology, Validation. **Sung-Ho Lee:** Formal analysis, Validation, Visualization, Writing - review & editing. **Neal Shah:** Investigation, Methodology, Validation. **Gabby Gerlach:** Investigation, Methodology, Validation. **Weiting Zhang:** Formal analysis, Investigation, Methodology, Validation, Visualization, Writing - review & editing. **Tzu-Hao Harry Chao:** Formal analysis, Investigation, Methodology, Validation, Visualization, Writing - review & editing. **Nathalie Van Den Berge:** Investigation, Methodology, Validation. **Carolyn Liu:** Methodology. **Carrie Donley:** Investigation, Methodology, Validation, Visualization. **Stephanie A. Montgomery:** Investigation, Methodology, Validation, Visualization, Writing - review & editing. **Yen-Yu Ian Shih:** Conceptualization, Data curation, Funding acquisition, Supervision, Project administration, Writing - original draft.

Declaration of Competing Interest
None.

barrier, we developed a simple, one-pot recipe to synthesize Carboxymethyl-dextran coated Iron Oxide Nanoparticles, namely, "CION", suitable for preclinical CBV-MRI applications. Here we disseminate a step-by-step instruction of our one-pot synthesis protocol, which allows CION to be produced in laboratories with minimal cost. We also characterized different CION-conjugations by manipulating polymer to metal stoichiometric ratio in terms of their size, surface chemistry, and chemical composition, and shifts in MR relaxivity and pharmacokinetics. We performed several proof-of-concept experiments *in vivo*, demonstrating the utility of CION for functional and structural MRI applications, including hypercapnic CO_2 challenge, visual stimulation, targeted optogenetic stimulation, and microangiography. We also present evidence that CION can serve as a cross-modality research platform by showing concurrent *in vivo* optical and MRI measurement of CBV using fluorescent-labeled CION. The simplicity and cost-effectiveness of our one-pot synthesis method should allow researchers to reproduce CION and tailor the relaxivity and pharmacokinetics according to their imaging needs. It is our hope that this work makes CBV-MRI more openly available and affordable for a variety of research applications.

Keywords

CION; Intravascular; Iron oxide; MRI contrast agent; fMRI; CBV; Angiography

Introduction

Blood-oxygenation-level-dependent functional MRI (BOLD-fMRI) is among the most commonly used noninvasive imaging techniques for functional brain mapping (Bandettini et al., 1992; Kim and Ogawa, 2012; Kwong et al., 1992; Logothetis, 2008; Ogawa et al., 1990, 1992; U urbil, 2012). This technique indirectly measures neuronal activity by detecting associated changes in regional blood oxygenation. In most cases, regional cerebral blood flow (CBF) increases adjacent to neuronal activity, resulting in a regional reduction of paramagnetic deoxyhemoglobin and subsequent enhancement of the BOLD-fMRI signal. Though BOLD-fMRI has been widely utilized, this technique suffers from low specificity and sensitivity. In preclinical animal models, cerebral blood volume (CBV)-weighted fMRI enhanced by exogenous contrast agents is a more sensitive alternative to BOLD (Kim et al., 2013; Lu et al., 2004b; Mandeville, 2012; Zhao et al., 2006). Additionally, CBV represents direct physiological changes to vascular tone, making this metric more easily interpretable. CBV-fMRI has been used for robust functional neuronal circuit mapping in preclinical animal models (Albaugh et al., 2016; Decot et al., 2017; Giorgi et al., 2017; He et al., 2018; Kim et al., 2013; Silva et al., 2007; Van Den Berge et al., 2017; Zhao et al., 2015, 2012), surgical planning (Cha, 2009; Nguyen et al., 2017), preoperative brain mapping in neurosurgical patients (Hart et al., 2016), clinical outcome assessment (Nasseri et al., 2014; Varallyay et al., 2018) and preclinical development of new therapeutic agents for various brain diseases (Artem Shatillo et al., 2020; Borsook et al., 2006; Carmichael et al., 2018). As this technique is capable of normalizing relaxivity changes to derive percent CBV changes, the resulting values can be independent of magnetic field strength and echo time, permitting comparisons across various acquisition settings (Fukuda et al., 2006; Harel et al., 2006; Jin and Kim, 2008b; Kim et al., 2013; Lu et al., 2004a, 2004c; Mandeville et al., 1998; Shih et al., 2014; Wu et al., 2004).

The first-ever CBV-fMRI study in human was conducted using serial injections of gadolinium chelate (Belliveau et al., 1991). Although this study demonstrated a significant task-induced vasodilation in primary visual cortex and set the foundation for MR-based functional brain mapping, the rapid washout of contrast required repeated dosing and thus lacked the much needed "steady-state" feature for efficient measurement. To date, most clinically-approved gadolinium-based contrast agents (GDCA) possess relatively short circulation half-life, which limits their use for fMRI applications. In addition, GDCA have been associated with long-term toxicity in the kidneys and brain (Gulani et al., 2017; Kuo et al., 2007; Malayeri et al., 2016; Wei et al., 2017). Development of MRI contrast agents based on superparmagnetic iron-oxide nanoparticles (SPIO, mean hydrodynamic diameter > 50 nm) or ultrasmall superparamagnetic iron-oxide nanoparticles (USPIO, mean hydrodynamic diameter 50 nm) have been increasingly used for diagnostic and theranostic purposes (Atanasijevic and Jasanoff, 2007; Atanasijevic et al., 2006; Chen et al., 2014, 2015; Himmelreich et al., 2005; Jung and Jacobs, 1995; Jung et al., 2014; Senpan et al., 2009; Shapiro et al., 2005, 2004; Stark et al., 1988; Wei et al., 2017; Weissleder et al., 1990a, 1990b; Wu et al., 2004). Careful manipulation of synthesis variables such as the size, magnetization and surface properties of SPIO/USPIO can be easily tailored to achieve longer intravascular half-life, higher MR sensitivity and better biocompatibility, as compared to commercially available GDCA. Typically composed of polymer-coated magnetite or maghemite nanocrystals, SPIO and USPIO-based nanoprobes can produce sensitive negative contrast via T_2 and T_2^* shortening that are usually stronger than GDCA (Atanasijevic et al., 2006; Bulte and Kraitchman, 2004). With GDCA and standard measurement conditions, 10–100 μM concentrations are typically required for robust visualization in MRI, whereas SPIO/USPIO based contrast agents are detectable at sub-micromolar concentrations (Atanasijevic et al., 2006). Unfortunately, except for Resovist® (FUJIFILM RI Farma Co., Ltd., Kyobashi, Tokyo, Japan) used for liver imaging in very few countries such as Japan, currently no FDA-approved iron-oxide contrast agent is available for clinical MRI (Daldrup-Link, 2017). Numerous first generation USPIO contrast agents such as Ferumoxtran-10 (Combidex®/Sinerem®), Feruglose (Clariscan™) or Supravist™ were withdrawn from the market following unfavorable safety profiles in phase II or III clinical trials (Wang, 2011).

Recently, most CBV-MRI studies were conducted with Ferumoxytol (Feraheme™), a second generation USPIO manufactured by AMAG pharmaceuticals, Inc. This formulation is comprised of an aqueous colloidal suspension of USPIO, coated with polyglucose sorbitol Carboxymethyl ether (PSC, a Carboxymethylated and reduced dextran composed of 20–22 glucose units) and made isotonic with mannitol (Bullivant et al., 2013). Although Feraheme has been clinically accepted for the parenteral therapy of iron-deficiency anemia in adult patients with chronic kidney diseases (Allkemper et al., 2002; Lu et al., 2010; Schiller et al., 2011), the FDA has not yet approved its use for MRI. Nevertheless, the long blood pool residence time of Feraheme has made it a preferred contrast agent for CBV mapping in a variety of preclinical models including rodents (Idée et al., 2006; Jung et al., 2014; Lu et al., 2005; Mueggler et al., 2001; Sieber et al., 2008; Weinstein et al., 2010, 2000; Weissleder et al., 1990b; Zhao et al., 2001), rabbits (Berry et al., 1996; D'Arceuil et al., 1999; Xia et al., 2014), cats (Zhang et al., 2010; Zhao et al., 2007, 2005) and nonhuman primates (Mandeville et al., 2001; Oliveira et al., 2016; Prince et al., 1995; Schroeter et al.,

2014). Feraheme has only been used in investigational 'off-label' high resolution magnetic resonance angiography (Hope et al., 2015; Stoumpos et al., 2018), resting state fMRI (D'Arceuil et al., 2013) and steady-state CBV mapping (Christen et al., 2013; Varallyay et al., 2013, 2018) in humans. Routine application of Feraheme in clinical and even preclinical settings is challenging due to numerous reasons. Firstly, to ensure patient safety, many research and clinical institutes as well as regulatory agencies in different countries may require an investigational new drug application to be approved for any 'off-label' application (Narang et al., 2013; Shi et al., 2013). Secondly, post marketing surveillance data has demonstrated the risk of serious and fatal hypersensitivity reactions including anaphylaxis in patients receiving Feraheme (Food and Administration, 2015; McCormack, 2012). In 2010, Takeda Pharmaceuticals was granted the right to develop and commercialize Ferumoxytol outside the US and its territories including Switzerland and the European Union (EU) under the trade name Rienso. Unfortunately, in 2015, the marketing authorization for Rienso was withdrawn in Europe at the mutual request of Takeda and AMAG pharmaceuticals due to commercial and regulatory reasons (Bullivant et al., 2013).

The sudden unavailability of Feraheme outside the US led to the suspension of many CBV-MRI studies in the field. Although some preclinical iron-oxide based nanoformulations are available in the market that could be used for CBV imaging, these formulations are relatively costly, especially considering the high doses required for *in vivo* MRI studies (15–30 mg/kg) (Albaugh et al., 2016; Decot et al., 2017; Giorgi et al., 2017; He et al., 2018; Kim et al., 2013; Silva et al., 2007; Van Den Berge et al., 2017; Zhao et al., 2015, 2012). Synthesizing a blood pool agent that simultaneously exhibit long shelf-life, high T_2 relaxivity and prolonged intravascular retention has proven challenging since *in vivo* efficacy and safety of nanoparticulate contrast agents depend on various parameters including size, magnetization, nature of surface functionality and polymer coverage on the surface of nanoparticles as well as their pharmacokinetics and biodistribution following intravenous administration (Arami et al., 2015; Hoshyar et al., 2016; Wang et al., 2015). In this study, we report a simple, one-pot recipe for the synthesis of **C**arboxymethyl-dextran coated **I**ron **O**xide **Na**noparticles, termed "**CION**", for reliable, preclinical MRI applications. We demonstrate methods to (1) tailor the material and pharmacokinetic properties of CION according to specific imaging requirements; (2) validate their suitability for various *in vivo* applications including high resolution micro-magnetic resonance angiography (μMRA) and stimulus-evoked CBV-fMRI; (3) evaluate their toxicity; and (4) conjugate CION with a fluorescent dye for cross-modality imaging. We also compared and validated our results against Feraheme. At the time of preparation of this manuscript, the cost of all equipment needed to perform in-house CION synthesis was ~ $3000 USD and the supplies/reagents needed to synthesize a batch of 150 ml of 20 mg Fe/ml CION is ~ $330 USD. The ease of production and cost-effectiveness of this CION synthesis protocol should make CBV-MRI platform openly accessible and affordable to preclinical MRI research laboratories.

Materials and methods

Synthesis of CION

Methods.—We synthesized CION using controlled, alkali-mediated co-precipitation of iron (III) chloride hexahydrate ($FeCl_3 \cdot 6H_2O$) and ammonium iron (II) sulfate [$FeSO_4 \cdot (NH_4)_2SO_4 \cdot 24\,H_2O$] in presence of Carboxymethyl-dextran (CMD) Sodium Salt (average molecular weight 10–20 kDa) (Fig. 1). All equipment, reagents/chemicals and laboratory supplies required for CION synthesis including their corresponding sources and tentative cost have been listed in Table S1. In order to determine the effect of reaction variables on the physicochemical and pharmacokinetic (PK) properties of CION, we initially prepared several formulations with varied stoichiometric ratio of CMD and iron-precursors. These compositions are designated as $CION_{120000}$, $CION_{60000}$, $CION_{30000}$, $CION_{17143}$ and $CION_{12000}$, where the numbers in subscript represents the theoretical molar ratio of total iron precursor to polymer used for the synthesis, considering the molecular weight of CMD to be 10 kDa. Among these, we selected three compositions to illustrate how the MR relaxivity and PK properties of CION are adjustable by changing reaction variables. Our step-by-step synthesis are described as follows, illustrated in Fig. 1, and further detailed in Supplementary Video 1.

1. Dissolve $FeCl_3 \cdot 6H_2O$ (4 mmol) and $(NH_4)_2Fe(SO_4)_2 \cdot 6H_2O$ (2 mmol) in 20 ml of de-ionized water deoxygenated via thermo-mechanical degasification prior to addition of the reagents. Stir the resulting solution at 800–1000 rpm and 80–90°C in a 250 ml beaker.

2. To synthesize $CION_{60000}$, $CION_{17143}$ and $CION_{12000}$, dissolve 1, 3.5 and 5 g of CMD, respectively in minimum volume of de-ionized water. Add the resultant solution slowly to the mixture of ferric and ferrous salt solution.

3. Initially, an orange precipitate would be observed, which would dissolve following the addition of 30% aqueous ammonia. Keep adding ammonia solution until all the precipitate dissolve and a silky, black colloid is obtained.

4. Add a Phosphate Buffered Saline (PBS) tablet to the resultant colloid for tonicity adjustment and stir the mixture for additional 3 h at 80°C to complete the nucleation and growth of nanoparticles.

5. Thereafter, cool the reaction mixture and centrifuge at 4000 rpm for 30 min in-order to facilitate separation of unreacted precursors and/or bigger particles, if any.

6. Transfer the nanoparticle solution to a Slide-A-Lyzer™ dialysis cassette/flask (Molecular weight cut-off: 20 kDa) and dialyze against PBS. Replace the dialysis media with fresh PBS every 2 h. After 24 h, transfer the colloidal suspension to a beaker and concentrate by evaporation on a hot plate at 40°C.

7. Adjust the final volume to approximately 20 mg Fe/ml theoretical concentration. Caution: Give special attention to the reaction mixture as soon as the volume reaches close to 15 mg Fe/ml to avoid gelling.

8. Sterilize the resultant colloid by passing through 0.2 μm PTFE syringe filters.

9. Transfer the final sterile solution was to a sterile vial.

10. Store the final formulation at room temperature.

Validation of CION

Physicochemical Characterization.—To demonstrate the physicochemical properties of CION resulting from the above-mentioned one-pot synthesis protocol, we provide characterization data using procedures detailed below.

Iron concentration.—Iron (Fe) concentration per milliliter (ml) for every synthesized batch of CION were determined using inductively coupled plasma mass spectrometry (ICP-MS) with a Nexion 300D ICP-MS equipped with collision cell and autosampler. Samples for ICP-MS analysis were directly submitted to the Nanomedicines Characterization Core Facility at the University of North Carolina (UNC) at Chapel Hill. To determine iron concentration per unit volume of the colloidal sample, a given volume of CION (50–100 μl) was digested with a given volume of concentrated nitric acid. Thereafter, a small portion of this digested sample was transferred to de-ionized water. ICP-MS data was acquired after further diluting this sample with DI water. Iron concentration in the analyte was determined by running a calibration curve with a known concentration of Fe. The intensity of the ^{57}Fe isotope was considered for quantification of Fe concentration. ICP-MS data was reported as concentration in ppb, which was converted into mg/ml and multiplied with total dilution factor to determine the amount of Fe present per unit volume of the contrast agent.

Size and morphology.—The size and morphology of nanoparticles were examined using a JEOL 2010F FAsTEM, a high-resolution transmission electron microscope (HRTEM) equipped with a 2KX2K Gatan CCD bottom mount camera and electron dispersive X-ray (EDX) attachment. The TEM samples were prepared by depositing a few drops of the respective nanoparticle preparations ultrasonically dispersed in water for 2 min on separate carbon-coated copper grids and air-dried at room temperature. An acceleration voltage of 200 kV and variable magnification (20kX–500kX) were used for imaging the samples. The hydrodynamic diameter (z-average) and polydispersity index (PDI) of the formulations were determined by dynamic light scattering (DLS) using a Malvern Zetasizer (Malvern Instruments, Malvern, UK). Hydrodynamic diameter measurements were performed in clear, disposable zeta cells, after diluting 1 μl of CION with 999 μl of DI water. Each sample was analyzed three times for a total period of analysis of 10 min. Samples with visible aggregation were not subjected to TEM or DLS analysis. Only nanoparticle preparations that were stable in physiologically compatible buffers at high concentrations (> 5 mg Fe/ml) for at least a week were characterized.

Surface chemistry and composition.—The surface chemistry of CION was studied using attenuated total reflection Fourier transform infrared (ATR-FTIR) spectroscopy using a Thermo Nicolet Nexux FTIR model 870 spectrometer. Measurements were done with colloidal samples. The surface composition of different CION preparations were obtained by X-ray photoelectron spectroscopy (XPS) using Al K_a excitation source in a Kratos Axis

Ultra DLD X-ray Photoelectron Spectrometer with a base pressure of *ca.* 6×10^{-9} torr. Pass energies of 80 eV and 20 eV were used for survey and high-resolution scans, respectively. Atomic concentrations were determined in the Kratos Vision software. Shirley backgrounds were used and the software calculated the area under each peak. Relative sensitivity factors were used to determine atomic concentrations using the Kratos Vision software.

MRI

Equipment.—All MRI studies were conducted using a Bruker 9.4 T/30-cm bore small animal MRI system. *In vitro* relaxometry studies were performed with a homemade sample holder and a quadrature transceiver volume coil with 35 mm inner-diameter. For *in vivo* rat MRI studies, animals were affixed on a homemade, custom-built holder and headpiece equipped with ear and tooth bars to minimize motion artifacts during imaging. A homemade surface coil (internal diameter ~1.6 cm) was placed directly over the head of the subject and used as a transceiver. Mouse imaging was performed on a commercial mouse holder using a 72 mm quad-transmit only volume coil and a quad-receive only mouse brain coil.

Animals.—All *in vivo* MRI studies and surgical procedures were conducted in accordance with the Guide for the Care and Use of Laboratory Animals, as adopted by the National Institutes of Health, and approved by UNC IACUC. Pharmacokinetic profile of different CION formulations as well as the suitability of $CION_{17143}$ for CBV-fMRI and multimodal applications were assessed on adult Sprague Dawley (SD) rats between 400 and 500 g weight ($n = 20$). The efficacy of $CION_{17143}$ as a μMRA contrast agent and its toxicity evaluation compared to Feraheme were tested on adult C57BL/6 J mice ($n = 11$) between 26 and 32 g of body weight.

In vitro Relaxometry.—Relaxometry of $CION_{60000}$, $CION_{17143}$ and $CION_{12000}$ and Feraheme were evaluated *in vitro* with a custom-designed sample holder (Fig. 3A) securing the samples in the volume coil. The samples tested were serially diluted and placed into a 1 ml syringe. From each test sample, we prepared 7 different Fe concentrations: 0 (saline), 3.48746E-06, 6.97491E-06, 1.74373E-05, 3.48746E-05, 6.97491E-05 and 0.000174373 M. Images of these phantoms were acquired using a standard spin-echo sequence featuring multiple repetition time (TR: 5000, 3000, 1500, 800, 400 and 200 ms) and echo time (TE: 11, 33, 55, 77 and 99 ms) with acquisition matrix of 256×256, field of view (FOV) of 40 mm^2, slice thickness of 1 mm, and 3 averages.

Pharmacokinetic MRI.—For pharmacokinetic (PK) assessment, each rat was anesthetized with urethane (1.3 g/kg) prior to experimentation. Throughout the experiment, heart rate and oxygen saturation (SpO_2) were continuously monitored using a non-invasive physiological monitoring system equipped with MR-compatible sensors and maintained within normal ranges (300–350 bpm and above 96%, respectively). Warm-water circulating pads were used to maintain rectal temperatures at 37±0.5 °C. After initial positioning and pre-scan adjustments, magnetic field homogeneity was optimized using Bruker FASTMAP shimming up to second order with an isotropic 7 mm^3 voxel encompassing the imaging slices. A fast-spin-echo T_2-weighted image was taken in the mid-sagittal plane to localize the anatomical position by identifying the anterior commissure at 0.36 mm posterior to bregma. For PK

assessment, we used a single shot gradient-echo (GE) echo-planar-imaging (EPI) sequence with acquisition matrix $= 80 \times 80$, FOV$= 2.56 \times 2.56$ cm, slice thickness$= 1$ mm, spectral bandwidth $= 250$ kHz, TR $= 1000$ ms, TE $= 8.3$ ms, flip angle $= 52°$. To ensure consistency of the imaging location, 8 coronal slices were acquired with the fourth anterior slice aligned with the anterior commissure. To monitor the clearance of CION from cerebrovasculature, EPI data was continuously acquired for 260 min and animals were intravenously injected with $CION_{60000}$ ($n = 2$), $CION_{17143}$ ($n = 5$), $CION_{12000}$ ($n = 3$) and Feraheme ($n = 3$) at a dose of 30 mg Fe/kg through a tail vein catheter at 20 min after scan onset.

In vivo fMRI applications.—Among all the CION formulations, only $CION_{17143}$ presented optimal physicochemical and pharmacokinetic properties for long-term vascular imaging applications (See *Results and Discussions* for details). To further verify if $CION_{17143}$ offers robust contrast for dynamic CBV-fMRI study, we performed several fMRI experiments including CO_2 challenge, visual stimulation, and optogenetic stimulation in adult SD rats. These studies employed well-established procedures with well-documented biological outcomes (Chan et al., 2017; 2012; Keilholz et al., 2006; Leong et al., 2016; Liang et al., 2015; Lin et al., 2008, 2009; Schmid et al., 2017, 2016; Wu et al., 2003; Yu et al., 2016; Zhao et al., 2005, 2006), and were not designed to address any specific biological or neural circuit related questions. Instead, we focused on demonstrating the utilization of CION for these experiments ($n = 1$ or 2 for each study). Animal preparations were similar to those recently published (Albaugh et al., 2016; Broadwater et al., 2018; Kao et al., 2014; Van Den Berge et al., 2017). Briefly, each rat was endotracheally intubated and ventilated with 1–1.5% isoflurane in medical air using a small animal ventilator (CWE Inc., SAR-830/PA, Armore, PA). Ventilation rate and volume were adjusted as required to maintain $EtCO_2$ within a range of 2.6–3.2% and SpO_2 above 96%. All other experimental protocols including animal monitoring, physiology maintenance, imaging hardware and pulse sequences were described in the PK measurement section. During all fMRI experiments, a cocktail of dexmedetomidine (0.1 mg/kg/h) and pancuronium bromide (1.0 mg/kg/hr) were infused intraperitoneally to the animals. The level of isoflurane anesthesia was lowered to 0.5% at 30 min after the start of infusion (Fukuda et al., 2013). All CBV-weighted fMRI data were acquired by the EPI protocol described in the Pharmacokinetic MRI section, with a bolus dose of $CION_{17143}$ (20 mg Fe/kg, i.v.) via a tail vein catheter. Specifically, these experiments include:

- **Hypercapnia-evoked fMRI with $CION_{17143}$**. To evaluate the effect of hypercapnia on steady-state CBV, animals were exposed to 5% CO_2 (in 95% air) challenge using a 180 s OFF, 180 s ON, and 360 s OFF paradigm post-CION injection.

- **Visual stimulation-evoked fMRI with $CION_{17143}$**. To evaluate the effect of visual stimulation, animals were exposed to 10 Hz blue light visual stimuli using a 40 s OFF, 10 s ON, and 40 s OFF paradigm repeating 8 times in a post-CION injection scan.

- **Optogenetic fMRI with $CION_{17143}$**. To stimulate pyramidal neurons in the motor cortex (M1), rats were microinjected with 1 μl of purified and concentrated adeno-associated virus ($\sim10^{12}$ infections units per ml, packaged

by the UNC Vector Core Facility) encoding channelrhodopsin-2 (ChR2) under Ca^{2+}/calmodulin-dependent protein kinase II promoter (CaMKIIa) and an enhanced yellow fluorescent protein (EYFP), or sham vector controls that do not express ChR2 ($n = 2$ each). Injection coordinate from bregma were anterior/posterior (AP): +3 mm, medial/lateral (ML): ±2.5 mm, and dorsal/ventral (DV): −1.5 mm. A control vector was injected into the M1 of the contralateral hemisphere. A 26-gauge injection needle connected to a 2 μl Hamilton syringe was used; each microinjection was performed over 10 min followed by another 10 min to allow diffusion of viral particles away from the injection site. After virus injection, chronic optical fibers were stereotactically implanted directly over the site of virus injection (DV: −1.0 mm) for light delivery. The time from virus injection to the start of the MRI experiments was 4–5 weeks. Before sending the animals inside the magnet, optical fibers were connected via 3 m patch cables to a solid-state laser (473 nm wavelength) located outside of the magnet room delivering ~10 mW light to virus-transfected region. We acquired stimulus-evoked fMRI data for 100 s during which light stimulation was applied in a 20 s OFF, 10 s ON, 30 s OFF, 10 s ON, and 30 s OFF paradigm. All subjects underwent 2–5 repeated trials at 40 Hz and 5 ms pulse width.

High resolution μMRA.—High resolution microangiography was performed in a C57Bl/6 J wild-type mouse anesthetized with 1.3 g/kg bolus of urethane (injected i.p. 1 h prior to imaging). We used a 3D Fast-Low-Angle-SHot (FLASH) sequence with acquisition matrix = 384×384×156, FOV = 19.2 × 19.2 × 7.8 mm, spectral bandwidth = 50 kHz, TR = 50 ms, TE = 5.9 ms, flip angle = 13°. This sequence allows mapping cerebrovasculature with an isotropic spatial resolution of 50 μm^3. Two separate acquisition (each with four repetitions) were acquired before and after CION$_{17143}$ injection (30 mg Fe/kg, i.v.), respectively.

Cross-modality application.—To demonstrate the utility of CION platform for cross-modality application, we conjugated CION with a red-fluorescent dye, Rhodamine B (Laser Grade, +99%, ACROS Organics™). Rhodamine B has been used for CBV measurement with two-photon microscopy (Tomita et al., 2011; Verant et al., 2007). Rhodamine B is usually conjugated with the antibiofouling polymer Dextran to prevent rapid bloodstream clearance. In this study, we conjugated Rhodamine B with CION with instead of Dextran, which not only endowed additional stability to the dye for optical measurements of local CBV with high temporal resolution (> 10 Hz), but also enabled brain-wide CBV mapping using simultaneous fMRI. Additionally, Rhodamine B can be measured simultaneously with a genetically encoded green fluorescent calcium indicator GCaMP6f—facilitating direct assessment of neuronal activity.

- **Animal Preparation and Surgery:** We expressed GCaMP6f in neurons of the forepaw area of the somatosensory cortex (coordinate from bregma: AP = +1.0, ML = +3.7, DV = −1.2 mm) in rats ($n = 4$) via an intracranial injection of genetically engineered Adeno-Associated Viruses (AAV9-Syn-GCaMP6f-WPRE-SV40, #100,837-AAV9, Addgene, Cambridge, MA). Rats were anesthetized initially by 5% isoflurane and maintained by a constant flow of 2–3% isoflurane mixed with medical air. Rectal temperature was continuously

monitored and maintained within 37 ± 0.5 °C using a feedback-controlled heating pad. Rats were head-fixed to a stereotactic frame (Kopf Instruments, Model 962, Tujunga, CA). An incision was made to the exposed skull surface and a burr hole were prepared at skull above the infusion coordinate. Microinjection was performed at a flow rate of 0.1 μl/min, and an additional 10 min was given for virus diffusion prior to slow retraction of the micro syringe needle. Subsequently, the incision was closed with 4.0 silk suture, and the rats were recovered from anesthesia. After two weeks of incubation, an optical fiber (#CFMLC12U-20, Thorlabs, Newton, NJ) was chronically implanted at a position that was at 0.3 mm above the virus injection site. Four MR-compatible miniature brass screws (Item #94070A031, McMaster Carr, Atlanta, GA) were anchored to the skull. Thereafter, the surface of the skull was covered with dental cement to seal implanted components and the wound was sutured to further protect the surgical site. Lidocaine jelly (#1,043,377, Henry Schein, Queens, NY) was applied around the surgical wound to relieve pain and prevent the rat from scratching the wound. Meloxicam (1.5 mg/kg for 2 days; #049,755, Henry Schein, Queens, N) was also given for further pain relief. Lincomycin hydrochloride (30 mg/kg, i.m.) was administrated to prevent infection. Rats were allowed at least 1 week for recovery before any further experiment.

- **Setting up the fiber-photometry system for simultaneous fMRI and optical imaging.** We used an established fiber-photometry setting (Meng et al., 2018) for concurrent fMRI applications. Briefly, we used a 488 nm continuous wave (CW) laser (OBIS 488LS-60, Coherent, Santa Clara, CA) to excite GCaMP6f, and a 561 nm CW laser (OBIS 561LS-60, Coherent, Inc.) to excite Rhodamine B. These two lasers were aligned, combined, and subsequently launched into a fluorescence cube (DFM1, Thorlabs, Newton, NJ). The fluorescence cube contained a dichroic mirror (ZT488/561rpc, Chroma Technology Corp) to reflect and launch the combined laser beam into the core of a multi-mode optical fiber patch cable (#M43L02, Thorlabs, Newton, NJ), which was connected to the chronically implanted optical fiber probe of rats. The emission fluorescence collected from the same fiber probe travelled back along the patch cable into the fluorescence cube, passed through the dichroic mirror and an emission filter (ZET488/561 m, Chroma Technology Corp, Bellows Falls, VT), and launched into the core of a multi-mode patch cable (M200L02S-A, Thorlabs, Newton, NJ) connected to a spectrometer (QE Pro-FL, Ocean Optics, Largo, FL). Spectral data was sampled at 10 Hz and processed using a UI software from Ocean View (Ocean Optics, Largo, FL). When trigger mode was setup in Ocean View, the spectrometer recording was synchronized with MRI TTL via an Arduino micro-controller board.

- **Simultaneous fMRI and fiber photometry in GCaMP6f rats.** The animal preparation for CBV-fMRI experiment was the same as aforementioned. Briefly, a pair of electrodes was inserted into the left forepaw between 2nd and 3rd / 3rd and 4th digits for electric stimulation. The stimulation paradigm was 60 s OFF - 30 s ON - 60 s OFF - 30 s ON - 60 s OFF. During the on blocks,

electric stimulation was applied using a constant current stimulation isolator (#A365RC, WPI, Sarasota, FL) with following parameters: 3 mA, 9 Hz, 0.5 ms pulse width. The stimulation isolator was synchronized with MRI using a National Instruments DAQ board to receive TTL triggers from MRI scanner, and send out stimulus triggers according to the stimulus paradigm set in a homemade program.

MRI data processing and analysis

Relaxometry.—*In vitro* relaxometric analyses were performed using a custom-written MATLAB (Math-Works, Natick, MA) script. Signal intensity corresponding to each Fe concentration at different TR and TE was extracted by placing identical size of region of interests (ROIs) on each phantom image. Relaxation curves for T_1 calculation was obtained by plotting signal intensities (SI) against variable TRs corresponding to the shortest TE. The T_1 recovery was plotted using a one phase exponential association fitting: SI = a*(1-exp($-b$*TR)) + c where a, b, c denotes the fitting parameters. Similarly, the T_2 values were obtained by plotting SI against variable TEs corresponding to the longest TR. The T_2 decay was plotted using a one phase exponential decay: SI = a*exp($-b$*TE). The relaxivity values (r_1= (1/ T_1)/[Fe] and r_2 = (1/ T_2)/[Fe]) were determined by linear fitting to the relaxation rates (1/ T_1 and 1/ T_2) *vs* Fe concentration [Fe].

Pharmacokinetics and Clearance.—All EPI data acquired for pharmacokinetic evaluation of CION were corrected for motion using Analysis of Functional Neuroimages (AFNI) software. Because the clearance of CION is a slow process with respect to our EPI temporal resolution, the time-series EPI data were smoothed by moving average using a 30 s sliding window to avoid noise influence on pharmacokinetic assessment. The resultant images were motion corrected, skull-stripped, and co-registered to a template space using custom-written Matlab scripts (Albaugh et al., 2016; Lai et al., 2015; Shih et al., 2013) and the Analysis of Functional Neuroimages (AFNI) program. Region of interest (ROI) was placed on the dorsal hippocampus and primary somatosensory cortex to extract the time-course data. The ΔR_2* values were calculated as follows: ΔR_2* $= -\frac{1}{TE}$ ln [S(t)/mean(S_o)], where S(t) represents the MR signal intensities over time and S_o represents the average signal intensity of baseline before CION injection. In order to accommodate for slight temporal delays due to manual CION injections, PK curves were aligned according to onset signal changes. To calculate various pharmacokinetic parameters, such as elimination constant (K_e) and half-life ($T_{1/2}$) of the contrast agent, we assumed that the maximum signal intensity change (ΔR_2*$_{max}$) caused by each CION formulation during the post-contrast injection period is directly proportional to the maximum (or peak) serum concentration that the contrast agent achieves in a specific compartment or test ROI. We assumed that the distribution and elimination of CION follows a one-compartmental model and accordingly, fit the decay of all contrast agents within a given ROI using a one-phase exponential decay model and ΔR_2*$_{max}$ as the initial value, *i.e. t* = 0. The pharmacokinetic profile of each CION was analyzed using the following equation:

$$Y = (Y_0 - \; Plateau) * exp(- \; K \times t) + \; Plateau$$

where, Y_0 is the Y value when t (time) is zero, Plateau is the Y value at infinite times, K is a rate constant expressed in reciprocal of the t axis time units. Except for $CION_{60000}$, which decays to a non-zero, steady plateau within two hours of contrast-agent administration, the Plateau was constrained to 0 for $CION_{17143}$, $CION_{12,000}$, and Feraheme, each of which tends to reach $Y = 0$ at infinite time.

fMRI data.—All EPI data acquired for pharmacokinetic evaluation of CION were slice-time corrected, motion-corrected, skull-stripped, and registered to the template space using AFNI. For the hypercapnia experiment, we performed an independent component analysis (ICA) and compared R_2^* derived between before and after the hypercapnic challenge. Signal before and after the initiation of the CO_2 challenge was compared using a two-sample *t*-test based on the response pattern identified from ICA. For the visual and optogenetic stimulation studies, a general linear model (GLM) with third-order polynomial regression was used. Benjamini–Hochberg's False discovery rate (FDR) correction procedure was applied for the multiple comparison (Benjamini and Hochberg, 1995). Finally, the imaging results have a threshold of $p < 0.01$ to demonstrate statistically significant clusters. To showcase functional relaxivity changes under CION, we did not normalize the signal to form percent CBV changes, but instead express all fMRI time-series data in R_2^*.

μMRA data.—3D FLASH image volumes were spatially co-registered using AFNI to correct for any spatial drift between repetitions using AFNI and averaged to improve signal-to-noise-ratio (SNR). Vascular contrast was made by subtracting data before and after $CION_{17143}$ administration. Brain were manually skull-stripped using ITK-SNAP and visualized using Amira (FE1, V5.3.3 or Avizo software, TGS, San Diego, CA, USA). Following masking only the blood vessels in the brain using Amira's segmentation editor, a 3D-rendering of the cerebrovasculature was overlaid on anatomical T_2-weighted images using Amira multi-plane viewer.

Toxicity, Biodistribution, and Histopathology.: To assess the biocompatibility of CION, toxicity studies were carried out in C57BL/6 J wild-type mice ($n = 5$). Mice were intravenously injected with CION at a higher 40 mg Fe/kg dose to examine biosafety in a wider dosing range. A separate group of mice ($n = 5$) was treated with Feraheme at the same 40 mg Fe/kg dose to serve as positive controls. General health and weight of animals were regularly monitored up to 7 days post-injection and humanely sacrificed with pentobarbital. All major organs such as liver, spleen, kidney, lungs and brain were immediately excised, submersion-fixed in 10% PFA for 72 h at 4 °C, processed on an ASP 6025 automated tissue processor (Leica Biosystems), and embedded in paraffin wax. Tissues were sectioned at 4 μm thick and mounted on glass slides. Tissue sections were deparaffinized prior to staining. Hematoxylin and eosin (H&E) staining was performed using pre-mixed hematoxylin, clarifier, bluing reagent, and eosin (Richard Allan Scientific). For Prussian blue staining, Gomori's method for iron staining was used, employing a 1:1 hydrochloric acid-Potassium ferrocyanide solution made from 20% hydrochloric acid and 10% potassium ferrocyanide, and a nuclear fast red counter stain. Immunohistochemistry for CD45 was performed on the Discovery Ultra (Ventana Medical Systems) using manufacturer reagents. Antigen retrieval was performed using CC1 pH 8.5. CD45 antibody (BD Pharmigen, Cat # 550,539) was used

at a final concentration of 1:2000 in Discovery PSS Diluent followed by anti-rat OmniMap HRP-conjugated antibody. Antigen detection was performed using Discovery Chromomap DAB, and nuclei were counterstained with Hematoxylin II and Bluing Reagent.

Statistical analysis

All data unless otherwise specified are expressed as mean ± standard error of the mean. Statistical analysis was performed with Graph Pad Prism 8.30. The hydrodynamic sizes, PDI and R_2*_{max} of various CION formulations were compared using a one-way analysis of variance (ANOVA). Multiple comparison tests were performed using Tukey-Kramer HSD post-hoc analyses. To compare the contrast properties between a pair of CION formulations at different time points, the R_2* values of a given formulation corresponding to baseline, as well as multiple post-injection periods were averaged. We performed two different types of comparison: (1) within group comparison to evaluate the averaged R_2* across different time points of a given formulation; and (2) inter-group comparison to compare the R_2* of different formulations at a particular time interval. Statistical analysis was performed using a two-way ANOVA, followed by Tukey's multiple comparison tests. $p < 0.05$ was used to denote statistical significance.

Results

CION synthesis and characterization.

The synthesis of CION has been schematically illustrated in Fig. 1 and further detailed in Video S1. We observed that CION synthesized with the molar ratio of Fe:CMD above 60,000:1 (assuming molecular weight of CMD = 10 kDa) were prone to agglomeration and therefore did not consider evaluating any higher ratios. In contrast, all nanoformulations synthesized with Fe:CMD ratio equal to or lower than 60,000:1 were stable in PBS with no visual aggregation for at least one month. The hydrodynamic diameter and PDI of CION synthesized with different Fe:CMD molar ratio are presented in Table S2. As the molar stoichiometric ratio of Fe:CMD decreased from 60,000:1 to 17,143:1, a statistically significant ($p < 0.0001$) decrease in the hydrodynamic size from 365.68 ± 5.04 nm to 50.65 ± 2.49 nm was observed. Concomitantly, a significant ($p < 0.01$) decrease in PDI from 0.423±0.021 to 0.240±0.018 was noted. Further reduction in Fe:CMD ratio (*e.g.* 12,000:1) had no significant effect on the PDI of nanoparticles though a notable ($p < 0.0001$) increase in hydrodynamic size occurred (96.30 ± 2.67 nm). Among all nanoformulations, $CION_{17143}$ presented the smallest hydrodynamic size ranging between 45 and 60 nm. We tested 4 different batches for reproducibility assessment and found the mean hydrodynamic diameter of the nanoparticles was 50.65 ± 2.49 nm and mean PDI was 0.2406±0.037 (Fig. S1). This nanoformulation did not show any visual aggregation in PBS for at least 6 months within a concentration of 10–30 mg Fe/ml. Fig. 2A presents the high resolution TEM images of $CION_{60000}$, $CION_{30000}$, $CION_{17143}$ and $CION_{12000}$. In all cases, nanoparticles were spherical or quasi-spherical in shape with particle size ranging between 5 and 10 nm. The electron dispersive X-ray spectrum of $CION_{17143}$ (Fig. S2) confirmed the presence of Fe, C and O in the sample. The ATR-FTIR spectrum of $CION_{17143}$ (Fig. 2B) displayed characteristic peaks at around 1105 cm^{-1} and 1015 cm^{-1}, ascribed to the presence of C–O bonds, and α-glucopyranose ring associated with the surface-dextran coat. The presence

of prominent stretching vibration band at 1637 cm^{-1} was indicative of the presence of carboxylic acid groups (–COOH) on the NP surface. Additionally, a broad band was observed in the frequency range of 3000–3500 cm^{-1}, ascribed to the –OH stretching vibration of –COOH and –OH functional moieties associated with the CMD surface-coat on iron-oxide. A typical survey XPS spectrum of $CION_{17143}$ is presented in Fig. 2C. The survey scan revealed the presence of C1s, O1s, Fe2p and Fe3p peaks at binding energy values of 285, 531, 710 and 725 eV. The high resolution C1s spectrum of $CION_{17143}$ (Fig. 2D) showed three distinct peaks at 285, 287 and 288 eV corresponding to the C–C, C–O and $C=O$ bonds inherent to chemical backbone of CMD present on the surface of CION. The Fe2p doublets with binding energy values of 710 and 725 eV (Fig. 2E) were representative of Fe-O bonds, typical of magnetite. We also used XPS to quantify the atomic concentrations of Fe, O and C on the surface of CION. Our results indicated that increasing the amount of polymer during co-precipitation reaction led to an increase in surface C:Fe atomic ratio (Fig. S3, Table S3).

In vitro relaxometry.

RepresentativeMR phantom images of $CION_{60000}$, $CION_{17143}$, $CION_{12000}$ and Feraheme acquired at different TRs and TEs using a custom-built holder (Fig. 3A) showed a concentration-dependent negative contrast enhancement when compared to saline control (Fig. 3B). The T_1 and T_2 relaxations of various CION compositions are presented in Fig. 3C. Among all the formulations tested, $CION_{60000}$ exhibited the highest r_2/r_1 ratio (r_1 = 3.173 mM^{-1}s^{-1}; r_2 = 1204 mM^{-1}s^{-1}) at 9.4T, followed by $CION_{12000}$ and $CION_{17143}$. The relaxivity of $CION_{17143}$ (r_1 = 1.412 mM^{-1}s^{-1}; r_2 = 109.8 mM^{-1}s^{-1}) was comparable to that of Feraheme (r_1 = 1.412 mM^{-1}s^{-1}; r_2 = 144.9 mM^{-1}s^{-1}) measured in this study as well as dextran-coated monocrystalline iron oxide nanoparticles (MION) reported by Zhao et al. at 9.4T (r_1 = 1–1.7 mM^{-1}s^{-1}; r_2 = 70–110 mM^{-1}s^{-1}) (Zhao et al., 2003).

In vivo Pharmacokinetics and Clearance.

Fig. 4A presents the $R_2{}^*$ signal change profile of $CION_{60000}$, $CION_{17143}$, $CION_{12000}$ and Feraheme on EPI scans of the rat brain. A two-way ANOVA examining the effect of all contrast agents on $R_2{}^*$ signal change in the hippocampus in 30 min intervals compared to baseline found a statistically significant interaction between the effects all contrast agents and the enhancement of $R_2{}^*$ signal compared to pre-contrast baseline ($F_{(3, 324)}$ = 216.6, $p < 0.0001$) in the 30 min following tail vein administration (Fig. 4B and C). $CION_{12000}$ and $CION_{60000}$ displayed rapid intravascular clearances with respective circulating half-lifes of 60.5 min and 14 min. $CION_{60000}$ had a rapid, one-phase exponential decay with R^{2*} reaching near baseline levels within 170 min of administration. In contrast, $CION_{17143}$ displayed an ideal pharmacokinetic profile for steady-state applications. A bolus, intravenous injection of $CION_{17143}$ increased the maximum $R_2{}^*$ to 102.342 ± 5.937 s^{-1} following administration, which was comparable to the maximum $R_2{}^*$ of Feraheme (p = 0.0636). Tukey-Kramer HSD *post-hoc* analysis indicated that $R_2{}^*$ change following $CION_{17143}$ administration remained statistically unaltered for the first hour (p = 0.0556). Using a one-phase, exponential decay model, the half-lives of $CION_{17,143}$ and Feraheme were calculated to be 472.3 min (7.87 h) and 468.4 min (7.81 h), respectively (Fig. S4). Because the $CION_{17143}$ and Feraheme exhibited linear-like pattern of clearance, we also

fit the clearance of both formulations using a linear regression and their slopes were found to statistically comparable ($p = 0.2186$; Fig. S5). Due to its long intravascular half-life, $CION_{17143}$ was selected for subsequent *in vivo* fMRI evaluations. The derivation of various pharmacokinetic parameters such as elimination constant (K_e) and half-life ($T_{1/2}$) from are shown in Fig. S4. Additionally, we also measured the R_2^* signal change profile for $CION_{60000}$, $CION_{17143}$, $CION_{12000}$ and Feraheme in the rat S1 cortex (Fig. S6).

In vivo fMRI applications.

We selected well-established fMRI procedures (Chan et al., 2017; 2012; Keilholz et al., 2006; Leong et al., 2016; Liang et al., 2015; Lin et al., 2008, 2009; Schmid et al., 2017, 2016; Wu et al., 2003; Yu et al., 2016; Zhao et al., 2005, 2006) to demonstrate the feasibility of using $CION_{17143}$ for fMRI with no intention to power the experiment to address any novel biological effects. Fig. 5 shows the use of $CION_{17143}$ in several common stimulus evoked-fMRI paradigms, including hypercapnic CO_2 challenge, visual stimulation, and targeted optogenetic stimulation. With the steady-state created by 20 mg/kg of $CION_{17143}$, 5% CO_2 challenge induced R_2^* increases throughout the brain, with the changes up to 15 s^{-1} (Fig. 5A). It should be noted that the CO_2-induced CBV-fMRI signal changes exhibited delayed onset and offset, likely attributed to the dead volume in the ventilator module or CO_2 delivery tubing as well as the time needed for the cerebral blood gas to respond to the different inhaled gases (*i.e.*, CO_2 or medical air). Visual stimulation at 10 Hz induced time-locked R_2^* increases throughout the rat visual network with robust activity in the superior colliculus (SC; Fig. 5B) and lateral geniculate nucleus (LGN; Fig. S7) with minimal activation in the mediomedial area of the secondary visual cortex (V2MM; Fig. S7). Optogenetic stimulation at 40 Hz induced R_2^* increases by 10 s^{-1} in the targeted primary motor cortex (M1) where Channelrhodopsin-2 (ChR2) was virally expressed (Fig. 5C).

High resolution μMRA.

To determine the utility of $CION_{17143}$ as a μMRA contrast agent, we performed a proof-of-concept experiment in a mouse. Fig. 6A presents the pre-and post-contrast FLASH-3D images of a mouse brain imaged at $100\mu m^3$ spatial resolution. The post-contrast image revealed the presence of several cerebral vessels in the cortical and subcortical regions not clearly visible prior to $CION_{17143}$ injection. Our findings identified similar vasculature observed in other μMRA studies using a similar USPIO-enhanced methodology (Fouquet et al., 2020; Klohs et al., 2012; Lin et al., 2013). The long intravascular half-life of $CION_{17143}$ enabled the acquisition of images at higher spatial resolution ($50 \mu m^3$ isotropic for the provided example). Fig. 6B shows the representative 3D cerebrovasculature of the mouse brain. We were able to identify several key arteries and veins from this dataset including rostral rhinal vein, galeno vein, collicular vein, transverse hippocampal arteries/veins, thalamostriate perforating arteries/veins, medial internal frontal artery, supracollicular arterial network, dorsal and medial cerebral arteries, lateral superior cerebella arteries and anterior medial striate artery.

Fluorescent-tagged CION for multimodal application.

To demonstrate the utility of CION platform for cross-modality application, we conjugated CION with Rhodamine B, a red-fluorescent dye, using the protocol shown in Fig. 7A and

Supplementary Materials, and administered this conjugate intravenously via tail vein in rats. Fig. 7B shows the photometry experimental setup and Fig. 7C shows photometry-measured normalized pharmacokinetic time-courses of Rhodamine-CION conjugate within 30 min after the injection and compares with injection of Rhodamine B alone (red) in the same animal with a few days apart. Notably, Rhodamine-CION appeared reaching a steady state faster than Rhodamine B alone. Rhodamine-CION also exhibited higher signal to noise ratio (SNR) than Rhodamine B (Fig. 7D). These data indicated that the conjugate was feasible, and Rhodamine-CION helped stabilize the pharmacokinetics, which should allow better CBV measurement using optical methods. To demonstrate a possible cross-modality application, we conducted simultaneous fMRI and fiber-photometry recording using the conjugated Rhodamine-CION with conventional forepaw electrical stimulation. Similar to prior *in vivo* application studies, we chose a well-established protocol to showcase the feasibility with no intention to address any novel biological effects thus did not fully power the experiment. Fig. 7E showed that GCaMP6f (neuronal calcium activity) and Rhodamine-CION (CBV) both increased during the stimulation period, and the CBV-fMRI time-course concurrently measured by Rhodamine-CION showed highly consistent pattern with the photometry CBV signal.

In vivo biocompatibility.

To study the biocompatibility of $CION_{17143}$, we examined toxicity using histology. $CION_{17143}$ was administered intravenously in mice at a higher dose of 40 mg Fe/kg and the results were compared with that from a separate group of mice receiving Feraheme injection at the same dose. As a preliminary step towards toxicity evaluation, we monitored the general health conditions of mice up to 7 days post-injection. We found no significant changes in body weight during the post-injection period (Fig. S8). While we did not systematically measure behavioral metrics in this study, our facility veterinary technicians on duty reported no pain or sickness behavior following $CION_{17143}$ treatment. All animals were sacrificed for histological assessment on day 7 after $CION_{17143}$ injection. H&E and Prussian blue staining, as well as CD45 labeling was performed on subsequent tissue sections to assess representative organ histopathology. The data were reviewed by a board-certified veterinary pathologist (S.A.M.) blinded to the treatment groups at time of analysis. As evident from both H&E as well as CD45 staining (Fig. 7), livers from both groups displayed mild lymphocytic inflammation, with the $CION_{17143}$ treated group displaying comparable, if not less inflammation than the Feraheme-treated group. Livers from both groups displayed similar amounts of extramedullary hematopoiesis, a common, nonspecific finding in mice. H&E findings of the kidney, spleen, brain, and lung in both groups exhibit normal feature. Prussian blue staining of the kidney revealed occasional iron deposition within the nephron, suggestive of renal filtration of the compounds. Prussian blue staining of spleens in both groups revealed moderate-numbers of iron-laden macrophages, which is expected in the spleen (a site of erythrocyte turnover) and is not ascribed to the treatment regimes.

Discussion

Over the past several years, many studies have proposed long-circulating, blood pool MR contrast agents (Zhou et al., 2017) synthesized by coating SPIO/USPIO with dextran or carboxymethyl dextran derivatives (Ayala et al., 2013; Creixell et al., 2010; Li et al., 2011; Liu et al., 2011; Sharma et al., 2018; Tassa et al., 2011; Wunderbaldinger et al., 2002; Groman et al., 2003), PEG-(Khandhar et al., 2017), PEG-derivatized phosphine oxide (Kim et al., 2011), PEGylated-silica (Wu et al., 2011) and bisphosphonate-anchored PEG (Sandiford et al., 2012). Many of these formulations such as crosslinked iron-oxides (CLIO) developed by Weissleder (Wunderbaldinger et al., 2002) or PEGylated-silica coated iron oxide nanoparticles developed by Wu et al. (2011) have shown promise for preclinical MRI application including cerebrovascular and cardiovascular imaging. However, these syntheses are based on a rather complex workflow that involves multi-step reactions with tedious purification steps and/or costly equipment and reagents, posing reproducibility and scaling-up challenges for laboratories lacking high-end chemistry resources. This study provides a detailed step-by-step guideline on how to synthesize an iron-oxide based MRI contrast agent from scratch using a streamlined and affordable protocol (Table S1). We also provide steps to tune the physicochemical properties of CION so that it can be made suitable for different types of *in vivo* applications. The simplicity of our one-pot method allows researchers to reproduce this method in their laboratories easily and tailor their nanoparticles according to their imaging needs by controlling reaction variables. For instance, $CION_{17143}$ is an ideal choice for steady-state CBV assessment due to its long intravascular half-life. However, the short-circulating $CION_{60000}$ may be best suited for applications such as imaging of liver, spleen, tumor. It might also find useful when selective targeting is needed for the contrast agent to flush out rapidly from the vascular compartments, leaving only targeted agent bound to disease-specific biomarkers. It is our hope that making our recipe publicly available will benefit chemists and MRI researchers to further advance the field.

To identify the optimal reaction conditions that can lead to maximum CMD grafting on nanoparticles while still having a decent iron payload per particle, a series of nanoformulations were formulated with varying stoichiometry of Fe to CMD. As observed by DLS, a decrease in Fe:CMD molar ratio from 60,000:1 to 17,143:1 led to a diminution in hydrodynamic size from 365.36 ± 5.04 nm to 50.65 ± 1.00 nm due to the increased polymer coating associated with nanoparticle surface, enhancing steric and electrostatic stabilization. But after a certain concentration of CMD in solution, the trend was reversed. Subsequently, a decrease in Fe: CMD molar ratio from 17,143:1 to 12,000:1 increased the nanoparticle size to 96.30 ± 2.67 nm. This observation is not surprising and may be attributed to depletion flocculation which occurs when the amount of polymer in the solution exceeds the threshold required to completely cover the surface of nanoparticles. When the excess polymer exists in the reaction mixture and the fully coated nanoparticles approach closer (*i.e.* less than the radius of gyration), the non-adsorbed free polymers between them are subject to exclusion due to entropic effects. Subsequently, the local concentration becomes lower than the surrounding level. The difference in concentration leads to an osmotic pressure difference, attracting two particles and eventually increasing the aggregate size. The TEM image of all nanoformulations prepared with Fe:CMD ratio between 60,000:1 to 12,000:1

showed hundreds of ultrafine, spherical to quasi-spherical particles with diameter ranging between 5 and 10 nm. Unlike DLS, an increase in the amount of coating agent during synthesis had nominal impact on the core size of nanoparticles. For all nanoformulations, particle sizes measured in TEM were at least 10–15 times smaller than their corresponding hydrodynamic sizes. This difference can be attributed to the differences in underlying principles involved in size measurement using these techniques. While TEM is used to image dry nanoparticles, DLS measures the size of hydrated nanoparticle, which include the contribution of the surface coating associated with the nanoparticle core and their solvation in the dispersion medium. The surface chemistry of CION was studied using ATR-FTIR spectroscopy. All tested nanoformulations (*i.e.* $CION_{60000}$, $CION_{17143}$ and $CION_{12000}$) presented identical spectral pattern except for increasing C–O stretching vibration intensity at around 1105, and 1015 cm^{-1}. The intensity of these bands can be qualitatively related to CMD functionalization density associated with the iron oxide core as we observed a smaller signal intensity for $CION_{60000}$ and a stronger intensity band for $CION_{12000}$ possessing a higher polymer content. We also observed a strong stretching vibration at 1637 cm^{-1} band, which was ascribed to the presence of carboxyl functionality associated with the CMD coat. This band, however, undergoes a hypsochromic (blue) shift when compared to the expected stretching region of carboxyl group, which is between 1700 and 1725 cm^{-1}. This blue shift, in part, could be contributed by the complexation of carboxyl groups on metal surface and/or presence of extensive hydrogen bonding between surface carboxyl groups. The presence of CMD coating on the surface of CION was further confirmed using XPS. As evident from the high resolution C1s XPS spectrum of $CION_{17143,}$ these NPs contained reactive carboxyl groups on their surface to allow further modification with functional biomolecules including proteins, antibodies, aptamers and therapeutic drugs. A thorough analysis of surface functionality and elemental composition using XPS conferred that the C:Fe atomic ratio on nanoparticles critically depended on the stoichiometric ratio of metal precursors to polymer used during nanoparticle synthesis.

To examine how variation of Fe:CMD molar ratio affects the relaxivity of nanoparticles, we measured the r_1 and r_2 for various CION compositions, namely, $CION_{60000}$, $CION_{17143}$ and $CION_{12000}$ using a conventional spin-echo based T_1 and T_2 mapping protocol. Among all the formulations, $CION_{60000}$ exhibited the highest r_2/r_1 ratio, followed by $CION_{12000}$ and $CION_{17143.}$ Two factors that determine the contrast enhancement of CIONs might help explain our results: (1) iron-oxide core (size and material); (2) thickness (coating and chemical composition). SPIO and USPIO are known to shorten T_2, which is governed by the translational diffusion of H_2O molecules in the inhomogeneous magnetic field surrounding the nanoparticles (Gillis and Koenig, 1987). According to quantum-mechanical outer sphere theory, the T_2 relaxivity of CION in solution can be expressed by the following equation:

$$1/T_2 = \left(256\pi^2\gamma^2/405\right)V * M_s^2 a^2/D(1 + L/a)$$

where γ denotes proton gyromagnetic ratio; V^*, M_s and a represented the volume fraction, saturation magnetization and the radius of iron oxide core, respectively; D is the diffusivity of water molecules, and L is the thickness of an impermeable surface coating (Brooks et al., 2001; Gillis et al., 2002; Tong et al., 2010). Of note, the coating molecules associated

with iron-oxide nanocore can result in exclusion of water from its surface, prevent water diffusion, or immobilize surrounding water molecules through formation of hydrogen bonds (Tong et al., 2010); all these factors can affect the nuclear relaxation of water protons. In this case, as the Fe:CMD ratio was lowered from 60,000:1 to 17,143:1, the hydrodynamic size of CION decreased with a concomitant increase in CMD coating thickness on the nanoparticle surface, resulting in a lower r_2/r_1 ratio, which was slightly less than Feraheme but greater than MION. However, a further increase in the amount of polymer during CION synthesis, increases the r_2/r_1 of CION. This observation, albeit off-the-trend, can be explained by an increased polymer coating thickness, which is supposed to have a deleterious effect on the saturation magnetization of the iron-core.

We evaluated the pharmacokinetic properties of three representative CION compositions – $CION_{60000}$, $CION_{17143}$ and $CION_{12000}$. Although intravenous injection of $CION_{60000}$ in rats led to reasonable contrast enhancement *in vivo*, our preliminary data indicated the half-life of this agent (11.2 min) was too short to meet prolonged imaging requirements, critical for several functional neuroimaging applications. This fast-clearing CION, however, can be well-suited for studies that have a shorter acquisition window such as liver and spleen imaging, cell-labeling and tumor targeting where fast clearance is essential to have unbound contrast agent removed from the vessels eliminating unnecessary background signal. Among all three formulations, $CION_{17143}$ presented the best results with regards to circulation stability ($T_{1/2} \sim 10$ h), while maintaining reasonable T_2* contrast *in vivo*. Our results indicated that the r_2 and intravascular half-life of $CION_{17143}$ is comparable to Feraheme, which makes it an ideal contrast agent for steady-state MRI applications. These results suggest that the molar ratio should not be too big or small to achieve long half-life, and an intermediate ratio (such as 17,143:1) could yield smaller hydrodynamic size and hence longer intravascular circulation.

We presented a few proof-of-concept fMRI studies. These studies were not intended to test the efficacy of our contrast agent in a large cohort and address specific neuroscience questions. Among these studies, hypercapnia or an elevated pCO_2 acts as a potent stimulator for vasodilation throughout the brain (Donahue et al., 2009; Faraci et al., 1994; Lu et al., 2009; Madden, 1993; Pollock et al., 2009; Yezhuvath et al., 2009), while visual stimulation in rodents increased activity in LGN and SC with variable responses ranging from increased to suppressed activation in visual cortices depending on the study design (Dinh et al., 2021; Jin and Kim, 2008a; Kim and Kim, 2011; Niranjan et al., 2016; Zhao et al., 2006). Using $CION_{17143}$, we were able to detect robust, site-specific R_2* changes in rats exposed to visual stimulation and hypercapnic challenge under lightly anesthetized conditions similar to those reported by others (Brevard et al., 2003; Dinh et al., 2021; Jin and Kim, 2008a; Lu et al., 2009; Niranjan et al., 2016). $CION_{17143}$ also demonstrated success in detecting robust optogenetic fMRI response in the cortical areas expressing ChR2 as expected (Lee et al., 2010; Ryali et al., 2016). Together, these results confirmed the efficacy of $CION_{17143}$ for fMRI applications. Due to its long plasma half-life and robust T_2 effects, this nanoformulation also showed excellent performance as a μMRA contrast agent, allowing improved visualization and delineation of cerebrovasculature *in vivo*. To validate the efficacy of CION for simultaneous fMRI and optical fiber photometry, we conjugated CION with a red fluorescent dye, Rhodamine B. The presence of reactive carboxyl groups

enabled facile immobilization of Rhodamine B on the surface of CION through a short, PEG-type spacer – 2,2′-(ethylenedioxy)-bis-(ethylamine) (EDEA) using well-established carbodiimide chemistry (Li et al., 2018). Although further characterizations are required to confirm the chemical structure of CION-rhodamine conjugate, our preliminary cross-modality experiments suggested that Rhodamine-labeled CION could serve as a platform for bridging tools across different spatiotemporal scales.

To determine the biocompatibility of $CION_{17143}$, we performed toxicity study in mice and compared the results with Feraheme. For toxicity analysis, we used a dose (40 mg/kg) that was higher than the highest dose (30 mg/kg) typically used for CBV-fMRI studies (Albaugh et al., 2016; Decot et al., 2017; Lai et al., 2015; Shih et al., 2013). We did not observe any abrupt changes in body weight up to 7 days post-injection; animals from both treatment group were apparently healthy and resumed their normal behavior and activities. Although H&E staining revealed the presence of mild lymphocytic inflammation in the livers from both treatment groups, the CION-treated group displayed slightly lower inflammation than Feraheme. For both treatment groups, no abnormalities were observed in the histopathological sections of kidney, spleen, brain and lung. To examine the biological fate of CION after 7 days post-administration, histopathological sections of liver, spleen, kidney, lungs and brain were also stained with Prussian blue, a common stain to detect the presence of iron in tissue specimens. Although we did not observe any iron accumulation in brain or lungs, iron deposits were visible in liver and spleen. This distribution profile is consistent with the proposed mechanism of iron metabolism for USPIO (Daldrup-Link, 2017). These results further indicate that both CION and Feraheme are eventually cleared from the intravascular space and enters the liver and spleen where they are most likely cleared by macrophages of the reticuloendothelial system (RES). As previously reported, it is possible that the nanoparticle coating is cleaved by lysosomal enzymes and the iron core is incorporated into the body's iron stores, where it is metabolized over 6–12 weeks. (AMAG Pharmaceuticals, 2017) Prussian blue staining of kidney also revealed minimal iron deposition within the nephron, indicating renal excretion of the nanoformulations. In summary, our results suggest that $CION_{17143}$ is a robust, reproducible, and safe steady-state contrast agent for preclinical MRI applications.

Conclusion

We developed a simple, inexpensive method to synthesize high-performance intravascular CION for MRI applications. By tuning the material and pharmacokinetic properties of CION through careful surface modulation, we formulated a blood pool agent that offers robust and stable contrast for high resolution CBV anatomical and functional imaging. Additionally, we developed and characterized other CION variants with shorter circulation half-life and high r_2/r_1 ratio; although these compositions cannot be used for steady-state imaging, they hold significant promise for liver or spleen imaging, cell labeling and/or tumor targeting *in vivo.* Finally, CION possesses a reactive carboxyl handle that enables conjugation with a variety of functional biomolecules and imaging entities. By labeling CION with a red fluorescent dye, Rhodamine B, we demonstrated the effectiveness of CION for simultaneous fMRI and optical fiber-photometry. Our future studies will focus on further optimization of

CION conjugate for various multimodal studies and developing new molecular MRI contrast agents using CION as the platform material.

Supplementary Material

Refer to Web version on PubMed Central for supplementary material.

Acknowledgment

Data/code availability statement

The raw and processed data required to reproduce these findings are available to download from https://data.mendeley.com/datasets/6mgrb9ttkn/2. CION samples may be available free-of-charge to the reader of this article for research purpose until supplies last. For more information, please visit https://camri.org or contact camri@unc.edu.

References

Albaugh DL, Salzwedel A, Van Den Berge N, Gao W, Stuber GD, Shih YYI, 2016. Functional magnetic resonance imaging of electrical and optogenetic deep brain stimulation at the rat nucleus accumbens. Sci. Rep6, 31613. [PubMed: 27601003]

Allkemper T, Bremer C, Matuszewski L, Ebert W, Reimer P, 2002. Contrast-enhanced blood-pool MR angiography with optimized iron oxides: effect of size and dose on vascular contrast enhancement in rabbits 1. Radiology223, 432–438. [PubMed: 11997549]

AMAG Pharmaceuticals, 2017. Inc. highlights of prescribing information for Feraheme. https://www.accessdata.fda.gov/drugsatfda_docs/label/2009/022180lbl.pdf.

Arami H, Khandhar A, Liggitt D, Krishnan KM, 2015. *In vivo* delivery, pharmacokinetics, biodistribution and toxicity of iron oxide nanoparticles. Chem. Soc. Rev44, 8576–8607. [PubMed: 26390044]

Artem Shatillo JR, Miettinen Tuukka, Keinanen Janika, Antti nurmi pharmacological MRI -*in vivo* imaging platform for pre-clinical CNS drug discovery. 2020https://www.criver.com/sites/default/files/resource-files/SP-SFN-17-pharmacological-mri-in-vivo-imaging.pdf.

Atanasijevic T, Jasanoff A, 2007. Preparation of iron oxide-based calcium sensors for MRI. Nat. Protoc2, 2582. [PubMed: 17948001]

Atanasijevic T, Shusteff M, Fam P, Jasanoff A, 2006. Calcium-sensitive MRI contrast agents based on superparamagnetic iron oxide nanoparticles and calmodulin. Proc. Natl. Acad. Sci103, 14707–14712. [PubMed: 17003117]

Ayala V, Herrera AP, Latorre-Esteves M, Torres-Lugo M, Rinaldi C, 2013. Effect of surface charge on the colloidal stability and *in vitro* uptake of carboxymethyl dextran–coated iron oxide nanoparticles. J. Nanopart. Res15, 1874. [PubMed: 24470787]

Bandettini PA, Wong EC, Hinks RS, Tikofsky RS, Hyde JS, 1992. Time course EPI of human brain function during task activation. Magn. Reson. Med25, 390–397. [PubMed: 1614324]

Belliveau J, Kennedy D, McKinstry R, Buchbinder B, Weisskoff R, Cohen M, Vevea J, Brady T, Rosen B, 1991. Functional mapping of the human visual cortex by magnetic resonance imaging. Science254, 716–719. [PubMed: 1948051]

Benjamini Y, Hochberg Y, 1995. Controlling the false discovery rate: a practical and powerful approach to multiple testing. J. R. Stat. Soc. Series B Methodol289–300.

Berry I, Benderbous S, Ranjeva JP, Gracia-Meavilla D, Manelfe C, Le Bihan D, 1996. Contribution of Sinerem® used as blood-pool contrast agent: detection of cerebral blood volume changes during apnea in the rabbit. Magn. Reson. Med36, 415–419. [PubMed: 8875412]

Borsook D, Becerra L, Hargreaves R, 2006. A role for fMRI in optimizing CNS drug development. Nat. Rev. Drug Discov5, 411. [PubMed: 16604100]

Brevard ME, Duong TQ, King JA, Ferris CF, 2003. Changes in MRI signal intensity during hypercapnic challenge under conscious and anesthetized conditions. Magn. Reson. Imaging21, 995–1001. [PubMed: 14684202]

Broadwater MA, Lee SH, Yu Y, Zhu H, Crews FT, Robinson DL, Shih YYI, 2018. Adolescent alcohol exposure decreases frontostriatal resting-state functional connectivity in adulthood. Addict. Biol23, 810–823. [PubMed: 28691248]

Brooks RA, Moiny F, Gillis P, 2001. On T2-shortening by weakly magnetized particles: the chemical exchange model. Magn. Reson. Med. Off. J.ournal of the Int. Soc. Magn. Reson. Med45, 1014–1020.

Bullivant J, Zhao S, Willenberg B, Kozissnik B, Batich C, Dobson J, 2013. Materials characterization of Feraheme/ferumoxytol and preliminary evaluation of its potential for magnetic fluid hyperthermia. Int. J. Mol. Sci14, 17501–17510. [PubMed: 24065092]

Bulte JW, Kraitchman DL, 2004. Iron oxide MR contrast agents for molecular and cellular imaging. NMR Biomed17, 484–499. [PubMed: 15526347]

Carmichael O, Schwarz AJ, Chatham CH, Scott D, Turner JA, Upadhyay J, Coimbra A, Goodman JA, Baumgartner R, English BA, 2018. The role of fMRI in drug development. Drug Discov. Today23, 333–348. [PubMed: 29154758]

Cha S, 2009. Neuroimaging in neuro-oncology. Neurotherapeutics6, 465–477. [PubMed: 19560737]

Chan RW, Leong AT, Ho LC, Gao PP, Wong EC, Dong CM, Wang X, He J, Chan Y–S, Lim LW, 2017. Low-frequency hippocampal–cortical activity drives brain-wide resting-state functional MRI connectivity. Proc. Natl. Acad. Sci114, E6972–E6981. [PubMed: 28760982]

Chang C, Lin CY, Chen JH, 2012. Three-dimensional microscopic magnetic resonance angiography. Google Patents.

Chen O, Riedemann L, Etoc F, Herrmann H, Coppey M, Barch M, Farrar CT, Zhao J, Bruns OT, Wei H, 2014. Magneto-fluorescent core-shell supernanoparticles. Nat. Commun5, 5093. [PubMed: 25298155]

Chen R, Romero G, Christiansen MG, Mohr A, Anikeeva P, 2015. Wireless magnetothermal deep brain stimulation. Science347, 1477–1480. [PubMed: 25765068]

Christen T, Ni W, Qiu D, Schmiedeskamp H, Bammer R, Moseley M, Zaharchuk G, 2013. High-resolution cerebral blood volume imaging in humans using the blood pool contrast agent ferumoxytol. Magn. Reson. Med70, 705–710. [PubMed: 23001902]

Creixell M, Herrera AP, Ayala V, Latorre-Esteves M, Pérez-Torres M, Torres-Lugo M, Rinaldi C, 2010. Preparation of epidermal growth factor (EGF) conjugated iron oxide nanoparticles and their internalization into colon cancer cells. J. Magn. Magn. Mater322, 2244–2250.

D'Arceuil H, Coimbra A, Triano P, Dougherty M, Mello J, Moseley M, Glover G, Lansberg M, Blankenberg F, 2013. Ferumoxytol enhanced resting state fMRI and relative cerebral blood volume mapping in normal human brain. Neuroimage83, 200–209. [PubMed: 23831413]

D'Arceuil HE, Crespigny AJD, Röther J, Moseley M, Rhine W, 1999. Serial magnetic resonance diffusion and hemodynamic imaging in a neonatal rabbit model of hypoxic–ischemic encephalopathy. NMR Biomed12, 505–514. [PubMed: 10668043]

Daldrup-Link HE, 2017. Ten things you might not know about iron oxide nanoparticles. Radiology284, 616–629. [PubMed: 28825888]

Decot HK, Namboodiri VM, Gao W, McHenry JA, Jennings JH, Lee SH, Kantak PA, Kao YCJ, Das M, Witten IB, 2017. Coordination of brain-wide activity dynamics by dopaminergic neurons. Neuropsychopharmacology42, 615. [PubMed: 27515791]

Dinh TNA, Jung WB, Shim HJ, Kim SG, 2021. Characteristics of fMRI responses to visual stimulation in anesthetized vs. awake mice. Neuroimage226, 117542. [PubMed: 33186719]

Donahue MJ, Stevens RD, De Boorder M, Pekar JJ, Hendrikse J, Van Zijl PC, 2009. Hemodynamic changes after visual stimulation and breath holding provide evidence for an uncoupling of cerebral blood flow and volume from oxygen metabolism. J. Cereb. Blood Flow Metabol29, 176–185.

Faraci FM, Breese KR, Heistad DD, 1994. Cerebral vasodilation during hypercapnia. Role of glibenclamide-sensitive potassium channels and nitric oxide. Stroke25, 1679–1683. [PubMed: 8042220]

Food U, Administration D, 2015. FDA drug safety communication: FDA strengthens warnings and changes prescribing instructions to decrease the risk of serious allergic reactions with anemia drug Feraheme (ferumoxytol).

Fouquet JP, Lebel R, Cahill LS, Sled JG, Tremblay L, Lepage M, 2020. Cerebrovascular MRI in the mouse without an exogenous contrast agent. Magn. Reson. Med84, 405–415. [PubMed: 31845401]

Fukuda M, Moon CH, Wang P, Kim SG, 2006. Mapping iso-orientation columns by contrast agent-enhanced functional magnetic resonance imaging: reproducibility, specificity, and evaluation by optical imaging of intrinsic signal. J. Neurosci26, 11821–11832. [PubMed: 17108155]

Fukuda M, Vazquez AL, Zong X, Kim SG, 2013. Effects of the a2-adrenergic receptor agonist dexmedetomidine on neural, vascular and BOLD fMRI responses in the somatosensory cortex. Eur. J. Neurosci37, 80–95. [PubMed: 23106361]

Gillis P, Koenig SH, 1987. Transverse relaxation of solvent protons induced by magnetized spheres: application to ferritin, erythrocytes, and magnetite. Magn. Reson. Med5, 323–345. [PubMed: 2824967]

Gillis P, Moiny F, Brooks RA, 2002. On T2-shortening by strongly magnetized spheres: a partial refocusing model. Magn. Reson. Med. Off. J. Int. Soc. Magn. Reson. Med47, 257–263.

Giorgi A, Migliarini S, Galbusera A, Maddaloni G, Mereu M, Margiani G, Gritti M, Landi S, Trovato F, Bertozzi SM, 2017. Brain-wide mapping of endogenous serotonergic transmission via chemogenetic fMRI. Cell Rep21, 910–918. [PubMed: 29069598]

Groman EV, Paul KG, Frigo TB, Bengele H, Lewis JM, 2003. Heat stable colloidal iron oxides coated with reduced carbohydrates and carbohdrate derivatives. Google Patents.

Gulani V, Calamante F, Shellock FG, Kanal E, Reeder SB, 2017. Gadolinium deposition in the brain: summary of evidence and recommendations. Lancet Neurol16, 564–570. [PubMed: 28653648]

Harel N, Lin J, Moeller S, Ugurbil K, Yacoub E, 2006. Combined imaging–histological study of cortical laminar specificity of fMRI signals. Neuroimage29, 879–887. [PubMed: 16194614]

Hart MG, Price SJ, Suckling J, 2016. Functional connectivity networks for preoperative brain mapping in neurosurgery. J. Neurosurg126, 1941–1950. [PubMed: 27564466]

He Y, Wang M, Chen X, Pohmann R, Polimeni JR, Scheffler K, Rosen BR, Kleinfeld D, Yu X, 2018. Ultra-slow single-vessel BOLD and CBV-based fMRI spatiotemporal dynamics and their correlation with neuronal intracellular calcium signals. Neuron97, 925–939 e925. [PubMed: 29398359]

Himmelreich U, Weber R, Ramos-Cabrer P, Wegener S, Kandal K, Shapiro EM, Koretsky AP, Hoehn M, 2005. Improved stem cell MR detectability in animal models by modification of the inhalation gas. Mol. Imaging4, 15353500200504196.

Hope MD, Hope TA, Zhu C, Faraji F, Haraldsson H, Ordovas KG, Saloner D, 2015. Vascular imaging with ferumoxytol as a contrast agent. Am. J. Roentgenol205, W366–W373. [PubMed: 26102308]

Hoshyar N, Gray S, Han H, Bao G, 2016. The effect of nanoparticle size on *in vivo* pharmacokinetics and cellular interaction. Nanomedicine11, 673–692. [PubMed: 27003448]

Idée JM, Port M, Raynal I, Schaefer M, Le Greneur S, Corot C, 2006. Clinical and biological consequences of transmetallation induced by contrast agents for magnetic resonance imaging: a review. Fundam. Clin. Pharmacol20, 563–576. [PubMed: 17109649]

Jin T, Kim SG, 2008a. Cortical layer-dependent dynamic blood oxygenation, cerebral blood flow and cerebral blood volume responses during visual stimulation. Neuroimage43, 1–9. [PubMed: 18655837]

Jin T, Kim SG, 2008b. Improved cortical-layer specificity of vascular space occupancy fMRI with slab inversion relative to spin-echo BOLD at 9.4 T. Neuroimage40, 59–67. [PubMed: 18249010]

Jung CW, Jacobs P, 1995. Physical and chemical properties of superparamagnetic iron oxide MR contrast agents: ferumoxides, ferumoxtran, ferumoxsil. Magn. Reson. Imaging13, 661–674. [PubMed: 8569441]

Jung H, Park B, Lee C, Cho J, Suh J, Park J, Kim Y, Kim J, Cho G, Cho H, 2014. Dual MRI T 1 and T 2 (*) contrast with size-controlled iron oxide nanoparticles. Nanomed. Nanotechnol. Biol. Med10, 1679–1689.

Kao YCJ, Li W, Lai HY, Oyarzabal EA, Lin W, Shih YYI, 2014. Dynamic perfusion and diffusion MRI of cortical spreading depolarization in photothrombotic ischemia. Neurobiol. Dis71, 131–139. [PubMed: 25066776]

Keilholz SD, Silva AC, Raman M, Merkle H, Koretsky AP, 2006. BOLD and CBV-weighted functional magnetic resonance imaging of the rat somatosensory system. Magn. Reson. Med. Off. J. Int. Soc. Magn. Reson. Med55, 316–324.

Khandhar A, Keselman P, Kemp S, Ferguson R, Goodwill P, Conolly S, Krishnan K, 2017. Evaluation of PEG-coated iron oxide nanoparticles as blood pool tracers for preclinical magnetic particle imaging. Nanoscale9, 1299–1306. [PubMed: 28059427]

Kim BH, Lee N, Kim H, An K, Park YI, Choi Y, Shin K, Lee Y, Kwon SG, Na HB, 2011. Large-scale synthesis of uniform and extremely small-sized iron oxide nanoparticles for high-resolution T 1 magnetic resonance imaging contrast agents. J. Am. Chem. Soc133, 12624–12631. [PubMed: 21744804]

Kim SG, Ogawa S, 2012. Biophysical and physiological origins of blood oxygenation level-dependent fMRI signals. J. Cereb. Blood Flow Metabol32, 1188–1206.

Kim SG, Harel N, Jin T, Kim T, Lee P, Zhao F, 2013. Cerebral blood volume MRI with intravascular superparamagnetic iron oxide nanoparticles. NMR Biomed26, 949–962. [PubMed: 23208650]

Kim T, Kim SG, 2011. Temporal dynamics and spatial specificity of arterial and venous blood volume changes during visual stimulation: implication for BOLD quantification. J. Cereb Blood Flow Metabol31, 1211–1222.

Klohs J, Baltes C, Princz-Kranz F, Ratering D, Nitsch RM, Knuesel I, Rudin M, 2012. Contrast-enhanced magnetic resonance microangiography reveals remodeling of the cerebral microvasculature in transgenic ArcAbeta mice. J. Neurosci32, 1705–1713. [PubMed: 22302811]

Kuo PH, Kanal E, Abu-Alfa AK, Cowper SE, 2007. Gadolinium-based MR contrast agents and nephrogenic systemic fibrosis. Radiology242, 647–649. [PubMed: 17213364]

Kwong KK, Belliveau JW, Chesler DA, Goldberg IE, Weisskoff RM, Poncelet BP, Kennedy DN, Hoppel BE, Cohen MS, Turner R, 1992. Dynamic magnetic resonance imaging of human brain activity during primary sensory stimulation. Proc. Natl. Acad. Sci89, 5675–5679. [PubMed: 1608978]

Lai HY, Albaugh DL, Kao YCJ, Younce JR, Shih YYI, 2015. Robust deep brain stimulation functional MRI procedures in rats and mice using an MR-compatible tungsten microwire electrode. Magn. Reson. Med73, 1246–1251. [PubMed: 24798216]

Lee JH, Durand R, Gradinaru V, Zhang F, Goshen I, Kim DS, Fenno LE, Ramakrishnan C, Deisseroth K, 2010. Global and local fMRI signals driven by neurons defined optogenetically by type and wiring. Nature465, 788. [PubMed: 20473285]

Leong AT, Chan RW, Gao PP, Chan YS, Tsia KK, Yung WH, Wu EX, 2016. Long-range projections coordinate distributed brain-wide neural activity with a specific spatiotemporal profile. Proc. Natl. Acad. Sci113, E8306–E8315. [PubMed: 27930323]

Li J, Zhou Y, Li M, Xia N, Huang Q, Do H, Liu YN, Zhou F, 2011. Carboxymethylated dextran-coated magnetic iron oxide nanoparticles for regenerable bioseparation. J. Nanosci. Nanotechnol11, 10187–10192. [PubMed: 22413363]

Li Y, Wang W, Wang Y, Zhang W, Gong H, Liu M, 2018. Synthesis and Characterization of rhodamine B-ethylenediamine-hyaluronan acid as potential biological functional materials. MSE359, 012040.

Liang Z, Liu X, Zhang N, 2015. Dynamic resting state functional connectivity in awake and anesthetized rodents. Neuroimage104, 89–99. [PubMed: 25315787]

Lin CY, Chang C, Cheung WM, Lin MH, Chen JJ, Hsu CY, Chen JH, Lin TN, 2008. Dynamic changes in vascular permeability, cerebral blood volume, vascular density, and size after transient focal cerebral ischemia in rats: evaluation with contrast-enhanced magnetic resonance imaging. J. Cereb. Blood Flow Metabol28, 1491–1501.

Lin CY, Lin MH, Cheung WM, Lin TN, Chen JH, Chang C, 2009. *In vivo* cerebromicrovasculatural visualization using 3D R2-based microscopy of magnetic resonance angiography (3D R2-mMRA). Neuroimage45, 824–831. [PubMed: 19154792]

Lin CY, Siow TY, Lin MH, Hsu YH, Tung YY, Jang T, Recht L, Chang C, 2013. Visualization of rodent brain tumor angiogenesis and effects of antiangiogenic treatment using 3D DeltaR2-muMRA. Angiogenesis16, 785–793. [PubMed: 23736837]

Liu G, Hong R, Guo L, Li Y, Li H, 2011. Preparation, characterization and MRI application of carboxymethyl dextran coated magnetic nanoparticles. Appl. Surf. Sci257, 6711–6717.

Logothetis NK, 2008. What we can do and what we cannot do with fMRI. Nature453, 869. [PubMed: 18548064]

Lu H, Golay X, Pekar JJ, Van Zijl PC, 2004a. Sustained poststimulus elevation in cerebral oxygen utilization after vascular recovery. J. Cereb. Blood Flow Metabol24, 764–770.

Lu H, Patel S, Luo F, Li SJ, Hillard CJ, Ward BD, Hyde JS, 2004b. Spatial correlations of laminar BOLD and CBV responses to rat whisker stimulation with neuronal activity localized by Fos expression. Magn. Reson. Med. Off. J. Int. Soc. Magn. Reson. Med52, 1060–1068.

Lu H, Patel S, Luo F, Li SJ, Hillard CJ, Ward BD, Hyde JS, 2004c. Spatial correlations of laminar BOLD and CBV responses to rat whisker stimulation with neuronal activity localized by Fos expression. Magn. Reson. Med52, 1060–1068. [PubMed: 15508149]

Lu H, Soltysik DA, Ward BD, Hyde JS, 2005. Temporal evolution of the CBV-fMRI signal to rat whisker stimulation of variable duration and intensity: a linearity analysis. Neuroimage26, 432–440. [PubMed: 15907301]

Lu J, Dai G, Egi Y, Huang S, Kwon SJ, Lo EH, Kim YR, 2009. Characterization of cerebrovascular responses to hyperoxia and hypercapnia using MRI in rat. Neuroimage45, 1126–1134. [PubMed: 19118633]

Lu M, Suh K, Lee H, Cohen M, Rieves D, Pazdur R, 2010. FDA review of ferumoxytol (feraheme) for the treatment of iron deficiency anemia in adults with chronic kidney disease. Am. J. Hematol85, 315–319. [PubMed: 20201089]

Madden JA, 1993. The effect of carbon dioxide on cerebral arteries. Pharmacol. Ther59, 229–250. [PubMed: 8278463]

Malayeri AA, Brooks K, Bryant LH, Evers R, Kumar P, Reich DS, Bluemke DA, 2016. NIH perspective on reports of gadolinium deposition in the brain. J. Am. Coll. Radiol. JACR13, 237. [PubMed: 26810815]

Mandeville JB, 2012. IRON fMRI measurements of CBV and implications for BOLD signal. Neuroimage62, 1000–1008. [PubMed: 22281669]

Mandeville JB, Jenkins BG, Kosofsky BE, Moskowitz MA, Rosen BR, Marota JJ, 2001. Regional sensitivity and coupling of BOLD and CBV changes during stimulation of rat brain. Magn. Reson. Med45, 443–447. [PubMed: 11241702]

Mandeville JB, Marota JJ, Kosofsky BE, Keltner JR, Weissleder R, Rosen BR, Weisskoff RM, 1998. Dynamic functional imaging of relative cerebral blood volume during rat forepaw stimulation. Magn. Reson. Med39, 615–624. [PubMed: 9543424]

McCormack PL, 2012. Ferumoxytol. Drugs72, 2013–2022. [PubMed: 22994536]

Meng C, Zhou J, Papaneri A, Peddada T, Xu K, Cui G, 2018. Spectrally resolved fiber photometry for multi-component analysis of brain circuits. Neuron98, 707–717 e704. [PubMed: 29731250]

Mueggler T, Baumann D, Rausch M, Rudin M, 2001. Bicuculline-induced brain activation in mice detected by functional magnetic resonance imaging. Magn. Reson. Med46, 292–298. [PubMed: 11477632]

Narang AS, Chang RK, Hussain MA, 2013. Pharmaceutical development and regulatory considerations for nanoparticles and nanoparticulate drug delivery systems. J. Pharm. Sci102, 3867–3882. [PubMed: 24037829]

Nasseri M, Gahramanov S, Netto JP, Fu R, Muldoon LL, Varallyay C, Hamilton BE, Neuwelt EA, 2014. Evaluation of pseudoprogression in patients with glioblastoma multiforme using dynamic magnetic resonance imaging with ferumoxytol calls RANO criteria into question. Neuro-oncology16, 1146–1154. [PubMed: 24523362]

Nguyen KL, Moriarty JM, Plotnik AN, Aksoy O, Yoshida T, Shemin RJ, Suh WM, Finn JP, 2017. Ferumoxytol-enhanced MR angiography for vascular access mapping before transcatheter aortic valve replacement in patients with renal impairment: a step toward patient-specific care. Radiology286, 326–337. [PubMed: 29040038]

Niranjan A, Christie IN, Solomon SG, Wells JA, Lythgoe MF, 2016. fMRI mapping of the visual system in the mouse brain with interleaved snapshot GE-EPI. Neuroimage139, 337–345. [PubMed: 27296012]

Ogawa S, Lee TM, Kay AR, Tank DW, 1990. Brain magnetic resonance imaging with contrast dependent on blood oxygenation. Proc. Natl. Acad. Sci87, 9868–9872. [PubMed: 2124706]

Ogawa S, Tank DW, Menon R, Ellermann JM, Kim SG, Merkle H, Ugurbil K, 1992. Intrinsic signal changes accompanying sensory stimulation: functional brain mapping with magnetic resonance imaging. Proc. Natl. Acad. Sci89, 5951–5955. [PubMed: 1631079]

Oliveira IS, Hedgire SS, Li W, Ganguli S, Prabhakar AM, 2016. Blood pool contrast agents for venous magnetic resonance imaging. Cardiovasc. Diagn. Ther6, 508. [PubMed: 28123972]

Pollock J, Deibler A, Whitlow C, Tan H, Kraft R, Burdette J, Maldjian J, 2009. Hypercapnia-induced cerebral hyperperfusion: an underrecognized clinical entity. Am. J. Neuroradiol30, 378–385. [PubMed: 18854443]

Prince MR, Narasimham DL, Stanley JC, Wakefield TW, Messina LM, Zelenock GB, Jacoby WT, Marx MV, Williams DM, Cho KJ, 1995. Gadolinium-enhanced magnetic resonance angiography of abdominal aortic aneurysms. J. Vasc. Surg21, 656–669. [PubMed: 7707570]

Ryali S, Shih YYI, Chen T, Kochalka J, Albaugh D, Fang Z, Supekar K, Lee JH, Menon V, 2016. Combining optogenetic stimulation and fMRI to validate a multivariate dynamical systems model for estimating causal brain interactions. Neuroimage132, 398–405. [PubMed: 26934644]

Sandiford L, Phinikaridou A, Protti A, Meszaros LK, Cui X, Yan Y, Frodsham G, Williamson PA, Gaddum N, Botnar RM, 2012. Bisphosphonate-anchored PEGylation and radiolabeling of superparamagnetic iron oxide: long-circulating nanoparticles for *in vivo* multimodal (T1 MRI-SPECT) imaging. ACS Nano7, 500–512. [PubMed: 23194247]

Schiller B, Bhat P, Sharma A, Li Z, Fortin G, McLaughlin J, Strauss W, 2011. Safety of Feraheme®(Ferumoxytol) in hemodialysis patients at 3 dialysis chains over a 1-year period. J. Am. Soc. Nephrol22, 477A–478A.

Schmid F, Wachsmuth L, Albers F, Schwalm M, Stroh A, Faber C, 2017. True and apparent optogenetic BOLD fMRI signals. Magn. Reson. Med77, 126–136. [PubMed: 26778283]

Schmid F, Wachsmuth L, Schwalm M, Prouvot P–H, Jubal ER, Fois C, Pramanik G, Zimmer C, Faber C, Stroh A, 2016. Assessing sensory versus optogenetic network activation by combining (o) fMRI with optical Ca2 + recordings. J. Cereb. Blood Flow Metabol36, 1885–1900.

Schroeter A, Schlegel F, Seuwen A, Grandjean J, Rudin M, 2014. Specificity of stimulus-evoked fMRI responses in the mouse: the influence of systemic physiological changes associated with innocuous stimulation under four different anesthetics. Neuroimage94, 372–384. [PubMed: 24495809]

Senpan A, Caruthers SD, Rhee I, Mauro NA, Pan D, Hu G, Scott MJ, Fuhrhop RW, Gaffney PJ, Wickline SA, 2009. Conquering the dark side: colloidal iron oxide nanoparticles. ACS Nano3, 3917–3926. [PubMed: 19908850]

Shapiro EM, Skrtic S, Koretsky AP, 2005. Sizing it up: cellular MRI using micron–sized iron oxide particles. Magn. Reson. Med. Off. J. Int. Soc. Magn. Reson. Med53, 329–338.

Shapiro EM, Skrtic S, Sharer K, Hill JM, Dunbar CE, Koretsky AP, 2004. MRI detection of single particles for cellular imaging. Proc. Natl. Acad. Sci101, 10901–10906. [PubMed: 15256592]

Sharma A, Cornejo C, Mihalic J, Geyh A, Bordelon DE, Korangath P, Westphal F, Gruettner C, Ivkov R, 2018. Physical characterization and *in vivo* organ distribution of coated iron oxide nanoparticles. Sci. Rep8, 4916. [PubMed: 29559734]

Shi Q, Pisani LJ, Lee YK, Messing S, Ansari C, Bhaumik S, Lowery L, Lee BD, Meyer DE, Daldrup-Link HE, 2013. Evaluation of the novel USPIO GEH121333 for MR imaging of cancer immune responses. Contrast Media Mol. Imaging8, 281–288. [PubMed: 23606432]

Shih YYI, Chen YY, Lai HY, Kao YCJ, Shyu BC, Duong TQ, 2013. Ultra high-resolution fMRI and electrophysiology of the rat primary somatosensory cortex. Neuroimage73, 113–120. [PubMed: 23384528]

Shih YYI, Huang S, Chen YY, Lai HY, Kao YCJ, Du F, Hui ES, Duong TQ, 2014. Imaging neurovascular function and functional recovery after stroke in the rat striatum using forepaw stimulation. J. Cereb. Blood Flow Metabol34, 1483–1492.

Sieber MA, Pietsch H, Walter J, Haider W, Frenzel T, Weinmann HJ, 2008. A preclinical study to investigate the development of nephrogenic systemic fibrosis: a possible role for gadolinium-based contrast media. Invest. Radiol43, 65–75. [PubMed: 18097279]

Silva AC, Koretsky AP, Duyn JH, 2007. Functional MRI impulse response for BOLD and CBV contrast in rat somatosensory cortex. Magn. Reson. Med. Off. J. Int. Soc. Magn. Reson. Med57, 1110–1118.

Stark DD, Weissleder R, Elizondo G, Hahn P, Saini S, Todd L, Wittenberg J, Ferrucci J, 1988. Superparamagnetic iron oxide: clinical application as a contrast agent for MR imaging of the liver. Radiology168, 297–301. [PubMed: 3393649]

Stoumpos S, Hennessy M, Vesey AT, Radjenovic A, Kasthuri R, Kingsmore DB, Mark PB, Roditi G, 2018. Ferumoxytol-enhanced magnetic resonance angiography for the assessment of potential kidney transplant recipients. Eur. Radiol28, 115–123. [PubMed: 28677065]

Tassa C, Shaw SY, Weissleder R, 2011. Dextran-coated iron oxide nanoparticles: a versatile platform for targeted molecular imaging, molecular diagnostics, and therapy. Acc. Chem. Res44, 842–852. [PubMed: 21661727]

Tomita Y, Pinard E, Tran-Dinh A, Schiszler I, Kubis N, Tomita M, Suzuki N, Seylaz J, 2011. Long-term, repeated measurements of mouse cortical microflow at the same region of interest with high spatial resolution. Brain Res1372, 59–69. [PubMed: 21111717]

Tong S, Hou S, Zheng Z, Zhou J, Bao G, 2010. Coating optimization of superparamagnetic iron oxide nanoparticles for high T2 relaxivity. Nano Lett10, 4607–4613. [PubMed: 20939602]

U urbil K, 2012. Development of functional imaging in the human brain (fMRI); the University of Minnesota experience. Neuroimage62, 613–619. [PubMed: 22342875]

Van Den Berge N, Albaugh DL, Salzwedel A, Vanhove C, Van Holen R, Gao W, Stuber GD, Shih YYI, 2017. Functional circuit mapping of striatal output nuclei using simultaneous deep brain stimulation and fMRI. Neuroimage146, 1050–1061. [PubMed: 27825979]

Varallyay CG, Nesbit E, Fu R, Gahramanov S, Moloney B, Earl E, Muldoon LL, Li X, Rooney WD, Neuwelt EA, 2013. High-resolution steady-state cerebral blood volume maps in patients with central nervous system neoplasms using ferumoxytol, a superparamagnetic iron oxide nanoparticle. J. Cereb. Blood Flow Metabol33, 780–786.

Varallyay CG, Nesbit E, Horvath A, Varallyay P, Fu R, Gahramanov S, Muldoon LL, Li X, Rooney WD, Neuwelt EA, 2018. Cerebral blood volume mapping with ferumoxytol in dynamic susceptibility contrast perfusion MRI: comparison to standard of care. J. Magn. Reson. Imaging48, 441–448. [PubMed: 29314418]

Verant P, Serduc R, Van Der Sanden B, Remy C, Vial JC, 2007. A direct method for measuring mouse capillary cortical blood volume using multiphoton laser scanning microscopy. J. Cereb. Blood Flow Metab27, 1072–1081. [PubMed: 17063147]

Wang J, Bai R, Yang R, Liu J, Tang J, Liu Y, Li J, Chai Z, Chen C, 2015. Size-and surface chemistry-dependent pharmacokinetics and tumor accumulation of engineered gold nanoparticles after intravenous administration. Metallomics7, 516–524. [PubMed: 25671498]

Wang YXJ, 2011. Superparamagnetic iron oxide based MRI contrast agents: current status of clinical application. Quant. Imaging Med. Surg1, 35. [PubMed: 23256052]

Wei H, Bruns OT, Kaul MG, Hansen EC, Barch M, Wi niowska A, Chen O, Chen Y, Li N, Okada S, 2017. Exceedingly small iron oxide nanoparticles as positive MRI contrast agents. Proc. Natl. Acad. Sci114, 2325–2330. [PubMed: 28193901]

Weinstein JS, Varallyay CG, Dosa E, Gahramanov S, Hamilton B, Rooney WD, Muldoon LL, Neuwelt EA, 2010. Superparamagnetic iron oxide nanoparticles: diagnostic magnetic resonance imaging and potential therapeutic applications in neurooncology and central nervous system inflammatory pathologies, a review. J. Cereb. Blood Flow Metabol30, 15–35.

Weissleder R, Elizondo G, Wittenberg J, Lee A, Josephson L, Brady T, 1990a. Ultrasmall superparamagnetic iron oxide: an intravenous contrast agent for assessing lymph nodes with MR imaging. Radiology175, 494–498. [PubMed: 2326475]

Weissleder R, Elizondo G, Wittenberg J, Rabito C, Bengele H, Josephson L, 1990b. Ultrasmall superparamagnetic iron oxide: characterization of a new class of contrast agents for MR imaging. Radiology175, 489–493. [PubMed: 2326474]

Westenberg JJ, van der Geest RJ, Wasser MN, van der Linden EL, van Walsum T, van Assen HC, de Roos A, Vanderschoot J, Reiber JH, 2000. Vessel diameter measurements in gadolinium contrast-enhanced three-dimensional MRA of peripheral arteries. Magn. Reson. Imaging18, 13–22. [PubMed: 10642098]

Wu EX, Tang H, Jensen JH, 2004. Applications of ultrasmall superparamagnetic iron oxide contrast agents in the MR study of animal models. NMR Biomed. Int. J. Devot. Dev. Appl. Magn. Reson. Vivo17, 478–483.

Wu EX, Wong KK, Andrassy M, Tang H, 2003. High-resolution *in vivo* CBV mapping with MRI in wild-type mice. Magn. Reson. Med. Off. J. Int. Soc. Magn. Reson. Med49, 765–770.

Wu SH, Lin CY, Hung Y, Chen W, Chang C, Mou CY, 2011. PEGylated silica nanoparticles encapsulating multiple magnetite nanocrystals for high-performance microscopic magnetic resonance angiography. J. Biomed. Mater. Res. Part B Appl. Biomater99, 81–88.

Wunderbaldinger P, Josephson L, Weissleder R, 2002. Crosslinked iron oxides (CLIO): a new platform for the development of targeted MR contrast agents. Acad. Radiol9, S304–S306. [PubMed: 12188255]

Xia J, Xie N, Feng Y, Yin A, Liu P, Zhou R, Lin F, Teng G, Lei Y, 2014. Brain Susceptibility weighted imaging signal changes in acute hemorrhagic anemia: an experimental study using a rabbit model. Med. Sci. Monit20, 1291. [PubMed: 25060330]

Yezhuvath US, Lewis-Amezcua K, Varghese R, Xiao G, Lu H, 2009. On the assessment of cerebrovascular reactivity using hypercapnia BOLD MRI. NMR Biomed. Int. J. Devot. Dev. Appl. Magn. Reson. Vivo22, 779–786.

Yu X, He Y, Wang M, Merkle H, Dodd SJ, Silva AC, Koretsky AP, 2016. Sensory and optogenetically driven single-vessel fMRI. Nat. Methods13, 337. [PubMed: 26855362]

Zhang N, Zhu XH, Zhang Y, Park JK, Chen W, 2010. High-resolution fMRI mapping of ocular dominance layers in cat lateral geniculate nucleus. Neuroimage50, 1456–1463. [PubMed: 20114078]

Zhao F, Holahan MA, Houghton AK, Hargreaves R, Evelhoch JL, Winkelmann CT, Williams DS, 2015. Functional imaging of olfaction by CBV fMRI in monkeys: insight into the role of olfactory bulb in habituation. Neuroimage106, 364–372. [PubMed: 25498426]

Zhao F, Jin T, Wang P, Hu X, Kim SG, 2007. Sources of phase changes in BOLD and CBV-weighted fMRI. Magn. Reson. Med57, 520–527. [PubMed: 17326174]

Zhao F, Wang P, Harel N, Nagaoka T, Kim S, 2003. Contrast agent-enhanced functional magnetic resonance imaging at 4.7 T and 9.4 T. In: Proceedings of the 11th ISMRM.

Zhao F, Wang P, Hendrich K, Kim SG, 2005. Spatial specificity of cerebral blood volume-weighted fMRI responses at columnar resolution. Neuroimage27, 416–424. [PubMed: 15923128]

Zhao F, Wang P, Hendrich K, Ugurbil K, Kim S–G, 2006. Cortical layer-dependent BOLD and CBV responses measured by spin-echo and gradient-echo fMRI: insights into hemodynamic regulation. Neuroimage30, 1149–1160. [PubMed: 16414284]

Zhao F, Welsh D, Williams M, Coimbra A, Urban MO, Hargreaves R, Evelhoch J, Williams DS, 2012. fMRI of pain processing in the brain: a within-animal comparative study of BOLD vs. CBV

and noxious electrical vs. noxious mechanical stimulation in rat. Neuroimage59, 1168–1179. [PubMed: 21856430]

Zhao M, Beauregard DA, Loizou L, Davletov B, Brindle KM, 2001. Non-invasive detection of apoptosis using magnetic resonance imaging and a targeted contrast agent. Nat. Med7, 1241–1244. [PubMed: 11689890]

Zhou Z, Bai R, Munasinghe J, Shen Z, Nie L, Chen X, 2017. T 1–T 2 dual-modal magnetic resonance imaging: from molecular basis to contrast agents. ACS Nano11, 5227–5232. [PubMed: 28613821]
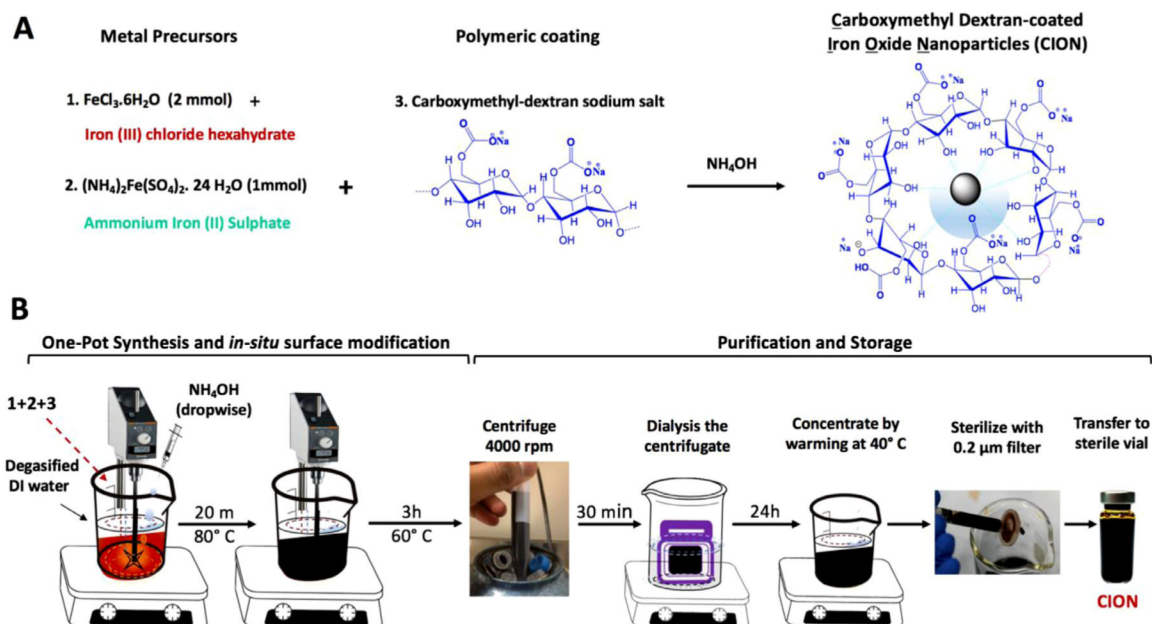
Fig. 1.
Synthesis of CION. **(A)** An illustration chemical conjugates used for CION synthesis. **(B)** A schematic methodology depicting the one-pot synthesis of CION via *in-situ*, alkali-mediated co-precipitation of metal precursors in presence of carboxymethyl dextran (CMD) sodium salt.
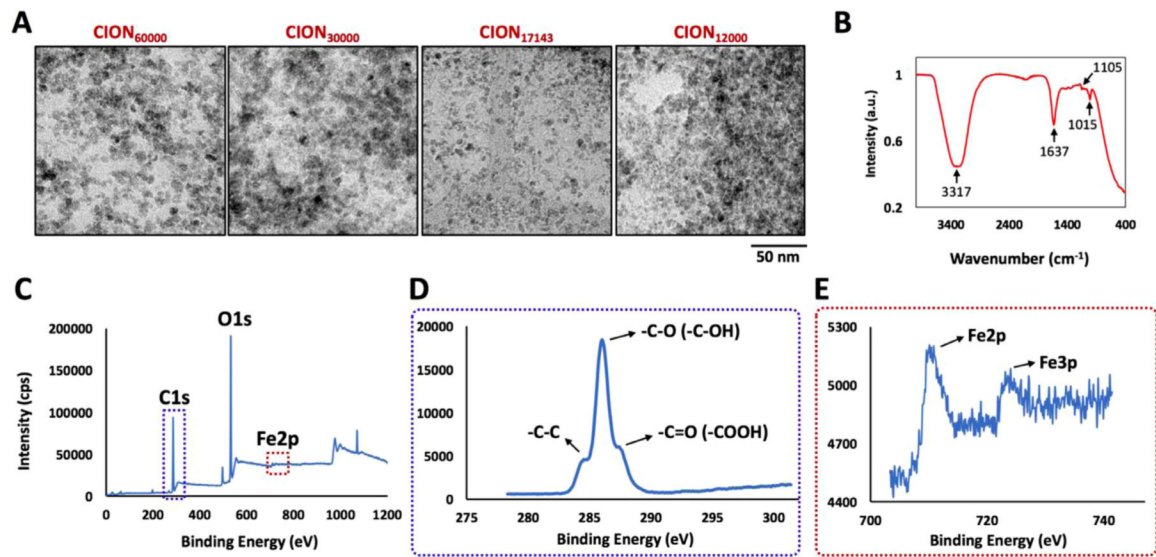
Fig. 2.
Physicochemical Characterization of CION. **(A)** Representative high-resolution TEM images of $CION_{60000}$, $CION_{30000}$, $CION_{17143}$ and $CION_{12000}$. **(B)** ATR-FTIR spectrum of $CION_{17143}$. **(C)** Full XPS spectrum for $CION_{17143}$ and isolated high-resolution XPS scans of **(D)** C1s and **(E)** Fe2p peaks.
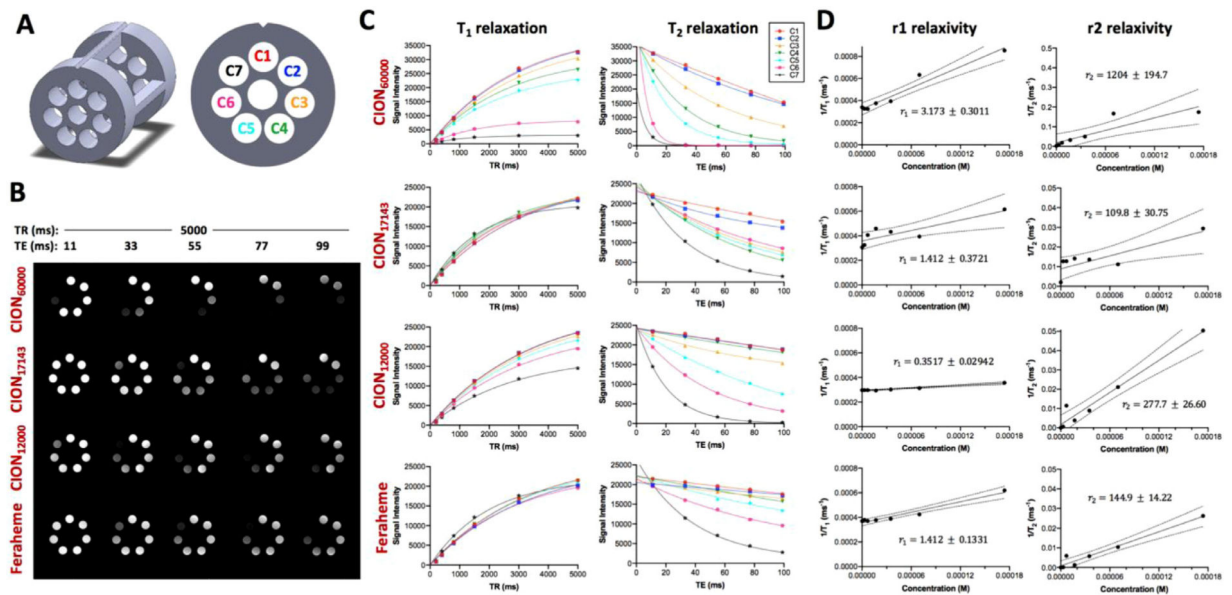
Fig. 3.
In vitro relaxometric analysis of CION. **(A)** Custom-design holder for relaxometric analysis. **(B)** Representative T_1- and T_2-weighted MR phantom images of various CION compositions and Feraheme acquired at different TR and TE. Note that this experiment collected a range of TR (5000, 3000, 1500, 800, 400 and 200 ms) and TE (11, 33, 55, 77 and 99 ms), but the figure only displays varying TE images with the longest TR due to space constraint. **(C)** T_1 and T_2 relaxation plots. **(D)** Quantification of r_1 and r_2.
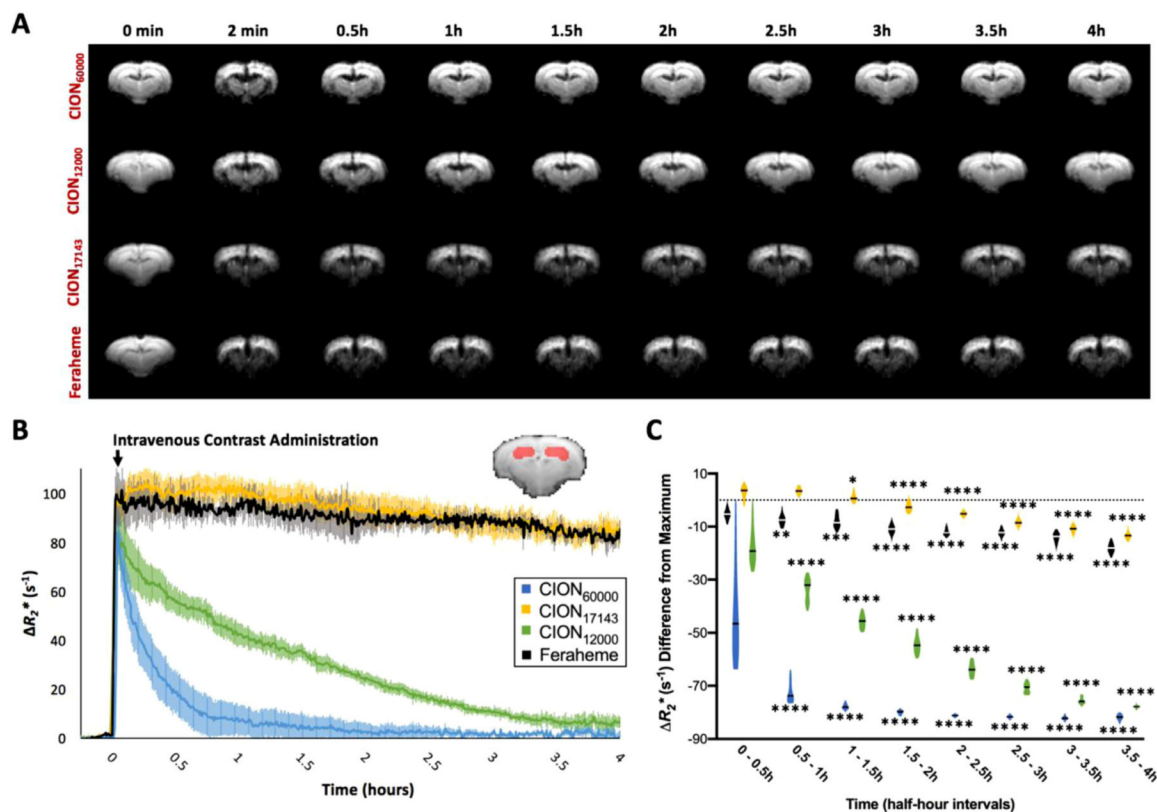
Fig. 4.

In vivo pharmacokinetic evaluation of CION conjugates and Feraheme in the rat brains. **(A)** Group-averaged EPI images of rat brains at various time points after $CION_{60000}$ (*n* = 3), $CION_{17143}$ (*n* = 6), $CION_{12000}$ (*n* = 4) and Feraheme (*n* = 3) administration. **(B)** Hippocampal R_2^* signal changes were evaluated up to 4 h following administration of each CION conjugate and Feraheme. **(C)** R_2^* signal decay from maximum contrast were calculated for every half-hour period and statistically compared to the first half-hour period for each contrast agent. *denotes $p<0.05$, **denotes $p<0.01$, ***denotes $p<0.001$, ***denotes $p<0.0001$.
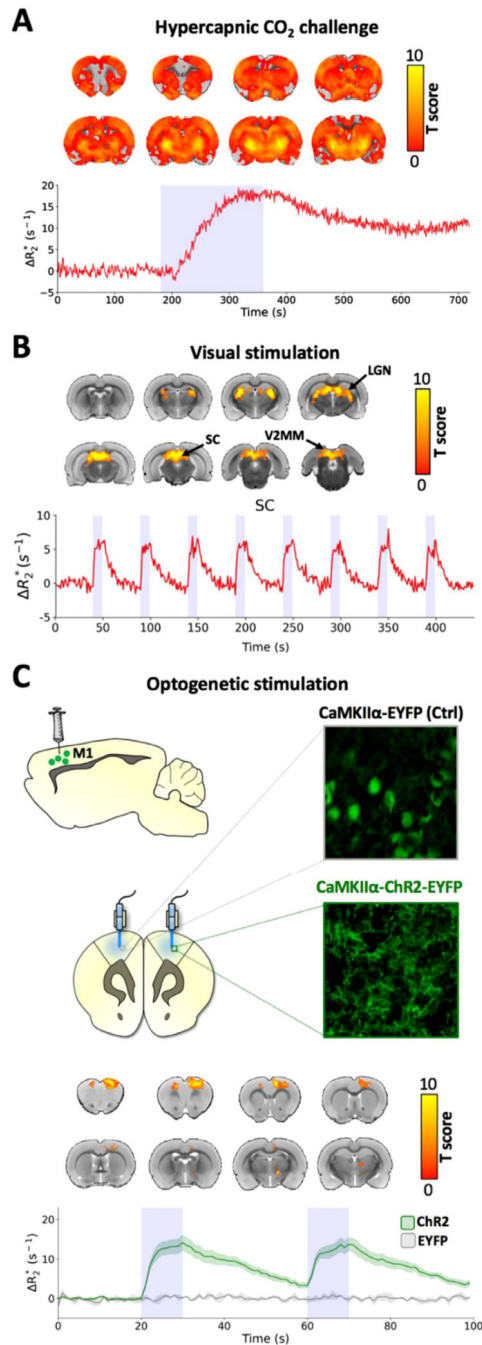
Fig. 5.

In vivo fMRI applications of $CION_{17143}$ in rats. **(A)** CBV activation map and global signal time-course R_2^* changes in response to hypercapnia. **(B)** Visual stimulation induces CBV activation along brain regions of the visual network and time-locked R_2^* changes in the SC in response to visual stimulation epochs (responses from additional ROIs shown in Supplemental Fig. S7). **(C)** Viral transfection of the control EYFP construct (left M1) produced a relatively uniform EYFP expression pattern consistent with the cytoplasmic cell-filling properties of the protein, while transfection of ChR2-EYFP (right M1) resulted in

a more diffuse EYFP expression pattern consistent with the trafficking and transmembrane characteristics of ChR2. CBV activation map and M1 time-course R_2^* changes in response to optogenetic stimulation. Threshold applied at $p < 0.05$ with FDR correction.
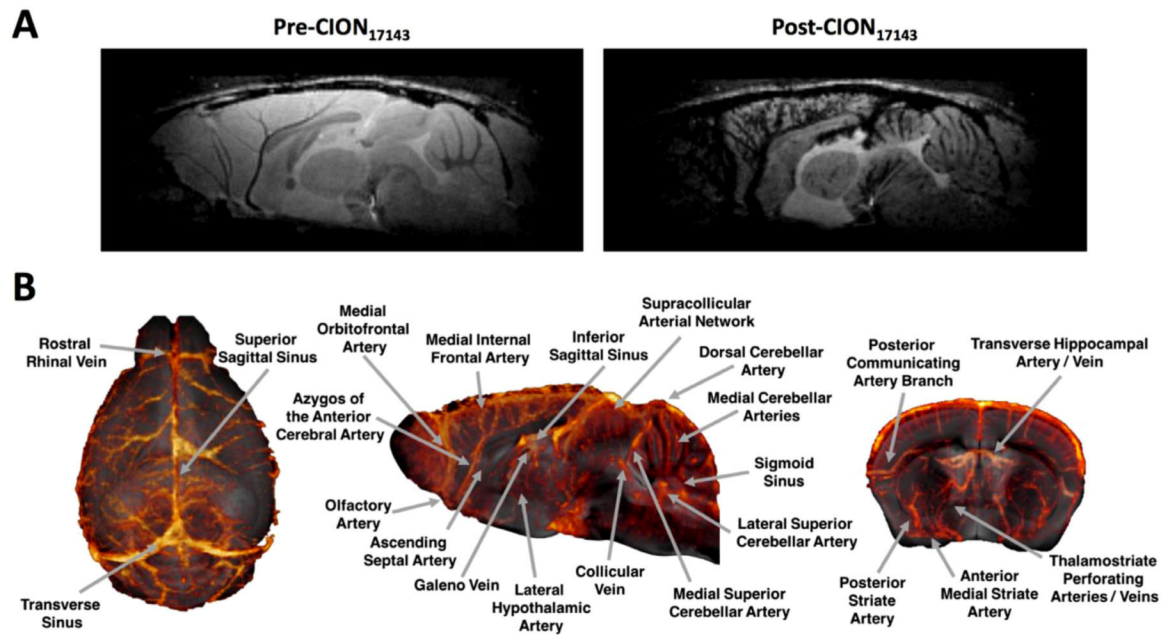
Fig. 6.
MR angiography using CION. **(A)** FLASH-3D images of mouse brain captured at 100 μm^3 spatial resolution before and after injection of $CION_{17143}$. **(B)** Representative 3D cerebrovasculature of the mouse brain generated from a post- and pre-contrast of FLASH 3D images acquired at 50 μm^3 spatial resolution.
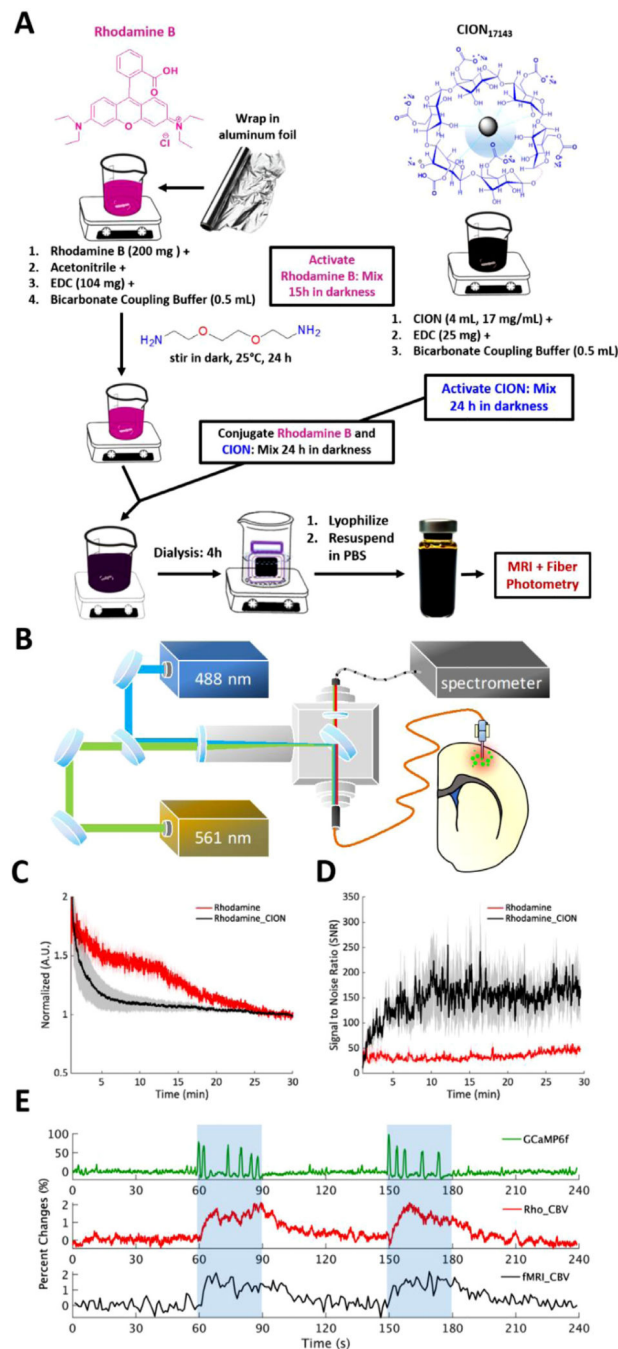
Fig. 7.
Concurrent fMRI-photometry application using fluorescent-labeled CION. **(A)** A schematic methodology depicting how $CION_{17143}$ is conjugated with the fluorescent Rhodamine B. **(B)** Fiber-photometry system uses two lasers to excite GCaMP (λ=488 nm) and Rhodamine (λ=561 nm), respectively, and a spectrometer to detect emitted photons changes over time. **(C)** Intravascular clearance measured by fiber-photometry ($n = 4$/contrast). Rhodamine-CION conjugate (black) shows faster stabilization to a steady-state compared to Rhodamine B (red). Note that the Y-axis represents a normalized intensity, thus a higher values of

Rhodamine B does not represent a stronger signal. **(D)** Signal-to-noise-ratio (SNR) of Rhodamine-CION conjugate is higher compared to Rhodamine B ($n = 4$/contrast). Error bars are standard error of the mean. Note that the Rhodamine-CION group shows a larger standard error, likely because it represents inter-subject variability. Indeed, the ratio of SNR and standard error was more comparable between Rhodamine and Rhodamine-CION groups. It should be noted that spontaneous activity fluctuation could also be amplified in Rhodamine-CION measurement, causing a larger SNR changes. **(E)** Concurrent fMRI and fiber-photometry recording (10 Hz sampling rate) shows increases in neuronal activity reflected by intercellular calcium release as well as CBV changes by both Rhodamine-CION conjugate fluorescence and fMRI-CBV measurement during forepaw electric stimulation (blue shading, 3 mA, 9 Hz, and 0.5 ms pulse width). (For interpretation of the references to color in this figure, the reader is referred to the web version of this article.).
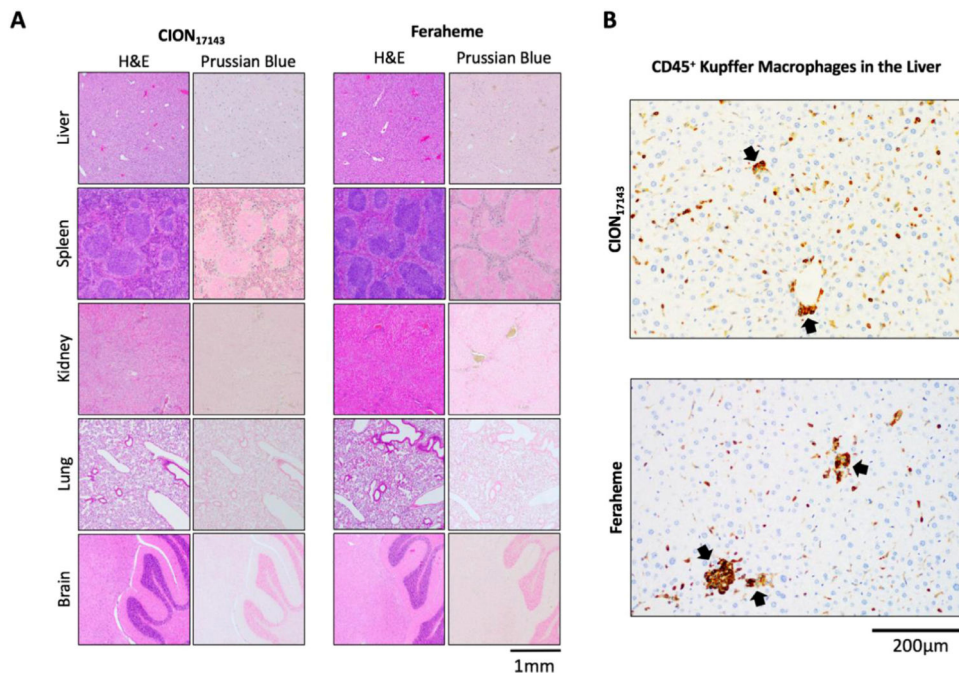
Fig. 8.
Toxicity and organ deposition of CION$_{17143}$ ($n = 5$) and Feraheme ($n = 5$) in mice 7 days after administration of a bolus 40 mg/kg dose. **(A)** Histological staining with H&E and Prussian Blue were conducted on sectioned liver, spleen, kidney, lung and brain showing no gross organ toxicity. Iron-deposition was restricted to cells in the liver and spleen. **(B)** Immunohistochemistry against CD45^{+} Kupffer macrophages in the liver revealed both CION$_{17143}$ and Feraheme displayed comparable mild lymphocytic inflammation (black arrows).